

**FACULTY
OF MATHEMATICS
AND PHYSICS**
Charles University

MASTER THESIS

Milan Peřta

Space-times of ring sources

Institute of Theoretical Physics

Supervisor of the master thesis: doc. RNDr. Oldřich Semerák, DSc.

Study programme: Physics

Study branch: Theoretical physics

Prague 2018

I declare that I carried out this master thesis independently, and only with the cited sources, literature and other professional sources.

I understand that my work relates to the rights and obligations under the Act No. 121/2000 Sb., the Copyright Act, as amended, in particular the fact that the Charles University has the right to conclude a license agreement on the use of this work as a school work pursuant to Section 60 subsection 1 of the Copyright Act.

In Prague, 20.7.2018

I would like to thank my supervisor, doc. RNDr. Oldřich Semerák, DSc., for his advice and guidance that he has provided during writing of this thesis, as well as over the years of my study at the Faculty of Mathematics and Physics of Charles University.

The completion of this thesis would not have been possible without the financial support from the grants GAČR 17-13525S of the Czech Science Foundation and GA UK 1176217.

Lastly, I am grateful to my family and girlfriend for always believing in me and I especially wish to thank my parents for their unconditional encouragement and support.

Title: Space-times of ring sources

Author: Milan Peřta

Institute: Institute of Theoretical Physics

Supervisor: doc. RNDr. Oldřich Semerák, DSc., Institute of Theoretical Physics

Abstract: Marginally outer-trapped surfaces (MOTSs) are found for a family of space-like hypersurfaces described by the Brill–Lindquist initial data. These hypersurfaces contain a singular ring characterized by its radius, mass and charge. Due to the ring character of the singularity, these surfaces are natural candidates for MOTSs with toroidal topology. By adjusting and employing the numerical method of geodesics, we indeed localize MOTSs of both spherical and toroidal topology, and compare the results with those obtained previously by Jaramillo & Lousto.

Keywords: general theory of relativity, black holes, apparent horizons, marginally trapped surfaces, ring sources

Contents

| | |
|--|-----------|
| Introduction | 2 |
| 1 Selected background from general relativity | 4 |
| 1.1 Notation | 4 |
| 1.2 Causal structure | 4 |
| 1.3 Congruences | 8 |
| 1.4 Initial value formulation | 10 |
| 1.5 Conformal transformations | 14 |
| 2 Black holes and singularities | 17 |
| 2.1 Trapped surfaces and apparent horizons | 18 |
| 2.2 Uniqueness theorems and topology of horizons | 19 |
| 3 Brill–Lindquist initial data | 21 |
| 3.1 Brill–Lindquist rings | 24 |
| 4 Numerical finding of apparent horizons | 27 |
| 4.1 Overview | 27 |
| 4.2 Basic algorithms | 28 |
| 4.3 Method of geodesics | 31 |
| 5 Properties of the Brill–Lindquist rings | 35 |
| 5.1 Numerical method | 35 |
| 5.2 Spherical MOTSs | 40 |
| 5.3 Toroidal MOTSs | 44 |
| 5.4 Final remarks | 54 |
| Conclusion | 57 |
| Bibliography | 59 |

Introduction

Since its publication in 1915 by Albert Einstein, the general theory of relativity has significantly changed how we understand space-time and the Universe. This geometric theory of gravitation predicts a number of phenomena which do not have analogy in classical physics, most notably the existence of extremely dense objects such that not even light can escape from their neighbourhood, and thus they appear black to an outer observer – hence the name black holes. Although these objects were considered to be mere mathematical peculiarities at first, it turned out that astrophysical systems like X-ray sources, active galactic nuclei and gamma-ray bursts are very probably driven by black holes. After a detailed study of our own galactic centre and an independent evidence provided by the recent first direct detections of gravitational waves, it seems beyond any reasonable doubt that black holes correspond to real astrophysical objects.

Naturally, the space-times of black holes have been largely studied, analytically as well as numerically. However, for more complicated situations than those of isolated stationary black holes in an asymptotically flat space-time, like for black holes interacting with other sources or/and for dynamical situations, it is still debated what a “black hole” actually means. Namely, there are several definitions of boundaries of black holes, called *horizons*, which are applicable in different situations and which do not always give the same answers. Indeed, in the literature there occur “counter-examples” to almost any of the definitions. Relatively “robust” is the notion of the *event horizon* which stems from the basic black-hole picture as a region from where it is not possible to escape. Event horizon has a number of favourable properties, e.g. smooth behaviour even in dynamical situations, but also one serious disadvantage: in order to localize it “at a given moment”, it is basically necessary to find all the history of a given space-time. This is not a problem in a stationary case, but in a dynamical case one better uses some quasi-local notion of a horizon, solely given by space-time properties in its small neighbourhood.

One of the questions which have not been fully clarified yet is whether under physically (or even astrophysically) relevant conditions the horizon *must* always have a spherical topology. Indeed, theoretically there might also exist toroidal horizons, but the “window” for their appearance is very narrow (see Section 2.2), and numerical simulations indicate that toroidal horizons occur very rarely, only in dynamical situations (gravitational collapse of matter with a suitable density distribution) and typically are very short-lived. An intuitive reason is that the gravitational pull can only be strong enough if its source is compact in all three spatial dimensions – whereas the toroidal horizon would necessarily have to be maintained by a line (ring-like) source. Admittedly, there do exist cylindrical horizons (in fact they are mostly employed to model the toroidal ones), but their host space-times typically have rather unphysical properties.

In this thesis, we numerically check whether horizons exist around massive charged infinitesimally thin (singular) ring sources. Such sources are natural candi-

dates for the appearance of toroidal horizons. We look for *apparent horizons* (more accurately, the so-called marginally outer-trapped surfaces) – a quasi-locally defined two-surfaces which should, roughly speaking, approximate the “snapshot” of the black-hole region in a given three-dimensional space-like hypersurface. Under quite generally accepted circumstances, apparent horizons always lie inside the event horizon or coincide with the latter, so they might be understood as an approximation of the event horizon “at a given instant”.

The thesis is organized as follows. After a general Introduction, we briefly summarize the necessary background from general relativity and geometry (Section 1). In Section 2, we specifically introduce the concepts concerning black holes (mainly marginally outer-trapped surfaces, or MOTSs for short and apparent horizons) which are then crucial in the original part of the thesis. In Section 3, we explain the Brill–Lindquist metrics – probably the simplest family of metrics describing the fields of massive charged ring singularities. Despite this simplicity, and the conceptual simplicity of MOTSs as well, the localization of the latter leads to rather tricky numerics, so we outline relevant algorithms in Section 4, with emphasis to time- and axially symmetric hypersurfaces. Choosing the numerical method of geodesics, we finally (in Section 5) localize the MOTSs in the above hypersurfaces and study the dependence of their arrangement on the parameters of the Brill–Lindquist sources. In particular, we confirm that both types of horizons – spheroidal and toroidal – exist (at least within certain parameter ranges) around the Brill–Lindquist rings. Finally, in Conclusion we summarize our results and compare them with those presented in the literature.

1. Selected background from general relativity

To understand the central idea of this thesis, the reader is supposed to master topics ranging from basic algebra to differential geometry, as well as their applications in general relativity. Hence, let us start with a minimal summary of the necessary topics to establish the right context for the chapters to follow.

1.1 Notation

In this thesis we use geometrized units in which the gravitational constant G and the speed of light c are set equal to one. Furthermore, we follow the abstract index notation of Wald (1984). That is, latin indices determine the covariant (lower index) or contravariant (upper index) character of a tensor, while greek indices correspond to the components of a tensor in the given basis. On top of that, purely spatial components are denoted by capital latin indices. Regarding tensor operations, the Einstein notation which implies summation over a repeated covariant and contravariant index is employed.

Space-time (M, g_{ab}) is assumed to be a four-dimensional smooth time-orientable manifold M with non-degenerate smooth symmetric metric tensor g_{ab} of signature $(-+++)$. Having introduced the metric tensor, it is possible to lower and raise indices,

$$V_a = g_{ab}V^b, \quad \omega^a = g^{ab}\omega_b, \quad (1.1)$$

where g^{ab} is the inverse metric. The covariant derivative compatible with g_{ab} is denoted by ∇_a as opposed to the partial derivative ∂_a and the Lie derivative \mathcal{L}_ξ along a vector field ξ^a . The Riemann tensor associated with the covariant derivative is defined by

$$\nabla_a \nabla_b \omega_c - \nabla_b \nabla_a \omega_c = R_{abc}{}^d \omega_d. \quad (1.2)$$

Finally, Ricci tensor R_{ab} is obtained by contracting the first and third index of the Riemann tensor, i.e.

$$R_{ab} = R^k{}_{akb}. \quad (1.3)$$

1.2 Causal structure

The causal structure of Minkowski space-time is rather intuitive and the reader is expected to be familiar with such concepts as light cones, causal future and causal past. Although the causal structure of space-time in general relativity is locally the same as in special relativity, significant differences can occur on a global scale due to nontrivial topology or space-time singularities. This section

aims to generalize these notions from special relativity, even for the case of curved space-times with such features. It should be noted, however, that the discussion regarding the causal structure is not limited merely to the case of solutions of the field equations. Quite on the contrary, it applies to an arbitrary space-time. More details on this topic can be found in Chapter 8 of Wald (1984), which we closely follow.

Let us first introduce basic definitions concerning futures and pasts. Consider an arbitrary space-time (M, g_{ab}) . At each point $p \in M$, the tangent vector space V_p to M is isomorphic to Minkowski space-time. We refer to the light cone passing through the origin of V_p as the light cone of p (note that it is a subset of V_p rather than of M). At each point p , we may label half of the light cone as “future” and the other half as “past”. Although there is a priori no reason to expect that a continuous designation of the future and the past can be made on the whole manifold, it is widely believed that such space-times which do not fulfill this requirement are of little physical importance. If a space-time does admit such a designation, it is said to be *time-orientable*. When determining the time-orientability of a given space-time, a useful result can be derived which relates the possibility of a continuous assignment of futures and pasts to the existence of a continuous nonvanishing time-like vector field. For convenience, we shall further restrict ourselves only to the case of time-orientable space-times.

Consider then such a space-time. We define a future directed time-like curve (FDTC) $\lambda(t)$ as a differentiable curve whose tangent vectors at each point $p \in \lambda$ are future directed time-like vectors (that is, each tangent vector lies in the future light cone of the given point). A future directed *causal* curve (FDCC) allows the tangent vectors to be both time-like and null. Analogous definitions can be made for past directed time-like and causal curves. Using the concepts of FDTCs and FDCCs, we define the chronological future $I^+(p)$ of $p \in M$ by

$$I^+(p) = \{q \in M \mid \exists \text{FDTC } \lambda(t) \text{ with } \lambda(0) = p \text{ and } \lambda(1) = q\}. \quad (1.4)$$

In other words, the chronological future of p is the set containing all such points q which can be reached from p by a FDTC. In general, $I^+(p)$ for each $p \in M$ is an open subset of M . The same holds for the chronological future of any subset S of M , denoted by $I^+(S)$, which is given by

$$I^+(S) = \bigcup_{p \in S} I^+(p). \quad (1.5)$$

The chronological pasts of any point p and any subset $S \subset M$ are denoted by $I^-(p)$ and $I^-(S)$, respectively, and definitions analogous to (1.4) and (1.5) apply.

The causal future $J^+(p)$ of p represents another useful concept. Its definition is the same as in the case of the chronological future (equation (1.4)), except that a FDTC is replaced by a FDCC, that is

$$J^+(p) = \{q \in M \mid \exists \text{FDCC } \lambda(t) \text{ with } \lambda(0) = p \text{ and } \lambda(1) = q\}. \quad (1.6)$$

$J^+(p)$ then constitutes the subset of M such that each $q \in J^+(p)$ can be reached from p by a FDCC. The causal future of any subset $S \subset M$ is thus the union of

the causal futures of all the points in S , i.e.

$$J^+(S) = \bigcup_{p \in S} J^+(p). \quad (1.7)$$

Again, the causal pasts $J^-(p)$ and $J^-(S)$ of any point $p \in M$ and any subset $S \subset M$ are defined in analogy with (1.6) and (1.7), with the word “past” replacing the word “future” everywhere. In contrast to $I^+(p)$, it always holds that $p \in J^+(p)$. A point is only contained in its own chronological future if there is a closed time-like curve beginning and ending at p . In general, $J^+(p)$ is not closed nor open. However, in globally hyperbolic space-times, it is always closed.

As mentioned at the beginning of this section, the causal structure of a general space-time locally coincides with that of Minkowski space-time. We shall now try to formulate this statement in a more precise, mathematically correct way. In the flat space-time, $I^+(p)$ consists of all the points that can be reached by future directed time-like geodesics starting from p and its boundary, denoted by $\partial I^+(p)$, is generated by future directed null geodesics radiating from the same origin. In an arbitrary space-time though, neither of these statements is generally true. Nevertheless, these results still hold locally in the sense of the following theorem formulated in Wald (1984) which we present without proof:

Let (M, g_{ab}) be an arbitrary space-time, and let $p \in M$. Then there exists a convex normal neighbourhood of p , i.e. an open set U with $p \in U$ such that for all $q, r \in U$ there exists a unique geodesic γ connecting q and r and staying entirely within U . Furthermore, for any such U , $I^+(p)|_U$ consists of all points reached by future directed time-like geodesics starting from p and contained within U , where $I^+(p)|_U$ denotes the chronological future of p in the space-time (U, g_{ab}) . In addition, $\partial I^+(p)|_U$ is generated by the future directed null geodesics in U emanating from p .

In addition to this theorem, it also holds that any causal curve connecting p to q for $q \in J^+(p) \setminus I^+(p)$ must be a null geodesic. Finally, it can also be shown that $\bar{I}^+(p) = \bar{J}^+(p)$ and $\partial I^+(p) = \partial J^+(p)$. Needless to say, all these results naturally extend to their past counterparts.

Before we define a globally hyperbolic space-time, a few more concepts have to be introduced. Consider a subset $S \subset M$, for which it holds $I^+(S) \cap S = \emptyset$. We shall call such a subset *achronal*. As it turns out, the boundary of the chronological future of a set has some nice properties related to the last definition as summarized in the following theorem (for proof see Wald, 1984):

Let (M, g_{ab}) be a time-orientable space-time, and let $S \subset M$. Then $\partial I^+(S)$ (if nonempty) is an achronal, three-dimensional, embedded, C^0 -submanifold of M .

Both the chronological and causal future of a set S can be viewed as a collection of events which could, in principle, be influenced by the events contained in the set. Let us now focus our attention on such sets of events which are completely determined by the events of S and, eventually, we will investigate when such sets correspond to the whole space-time. First, assume a time-orientable space-time (M, g_{ab}) and its closed achronal subset $S \subset M$. The edge of S is defined as the

set of all such points $p \in S$ that every open neighbourhood O of p contains a point $q \in I^+(p)$, a point $r \in I^-(p)$ and a time-like curve from r to q which does not intersect S . It should be noted that there are closed achronal sets without edge. We further present a useful theorem (as stated in Wald, 1984):

Let S be a (nonempty) closed achronal set with $\text{edge}(S) = \emptyset$. Then S is a three-dimensional, embedded, C^0 -submanifold of M .

Consider now a closed achronal set S with typically non-empty edge. The future domain of dependence of S , denoted by $D^+(S)$ is defined as follows

$$D^+(S) = \left\{ p \in M \mid \begin{array}{l} \text{Every past inextendible causal curve} \\ \text{through } p \text{ intersects } S \end{array} \right\}. \quad (1.8)$$

To understand this definition, it is essential to extend the definitions of future directed time-like and causal curves from the differentiable to the continuous case. Loosely speaking, a curve is called continuous if, locally, it is possible to connect pairs of points on the curve by a differentiable curve. A continuous curve λ is then a future directed time-like or causal curve if for each $p \in \lambda$ there is a convex normal neighbourhood U of p such that if $\lambda(t_1), \lambda(t_2) \in U$ with $t_1 < t_2$, then there is a future directed time-like or causal *differentiable* curve in U from $\lambda(t_1)$ to $\lambda(t_2)$.

In addition, the notion of extendibility is crucial in order to distinguish between the possibilities that a curve “runs off to infinity” or “runs around in circles” or ends at a singularity, as opposed to the case when it merely ends because we did not define it to go any further. This can be done using the concept of an *endpoint* of a curve. Consider a future directed causal curve λ . We say that λ has a future endpoint if there is a point $p \in M$ (in general, $p \notin \lambda$) such that for every neighbourhood O of p there exists t_0 so that $\lambda(t) \in O$ for every $t > t_0$. Apparently, by the Hausdorff property of M , there can be maximally one future endpoint of a future directed causal curve. A curve which has no future endpoint is then called future inextendible. Past inextendibility is defined in an analogous way. Note that a future directed causal differentiable curve with an endpoint may not be extendible as a differentiable causal curve but it is always extendible as a continuous causal curve.

Having introduced the future domain of dependence $D^+(S)$ of a closed achronal set S , it can be shown that it always holds $S \subset D^+(S) \subset J^+(s)$. The set $D^+(S)$ is an important concept since, provided that nothing travels faster than light, any event $q \in D^+(S)$ is fully determined by the information contained in S , which is a desired property of a theory when formulating the initial value problem. The past domain of dependence $D^-(S)$ of S is defined by replacing the word “future” with the word “past” in (1.8). The (full) domain of dependence $D(S)$ is then the union of $D^+(S)$ and $D^-(S)$, i.e.

$$D(S) = D^+(S) \cup D^-(S). \quad (1.9)$$

Hence, the domain of dependence of a closed achronal set corresponds to all the events in M whose conditions are completely determined by the events contained in the set. Consider now such a closed achronal set Σ for which it additionally

holds $D(\Sigma) = M$. This set is known as a *Cauchy surface* and it is straightforward to show that $edge(\Sigma) = \emptyset$. Furthermore, by the theorems presented in this section, every Cauchy surface is an embedded C^0 -submanifold of M . Finally, a space-time containing a Cauchy surface is said to be *globally hyperbolic*. As it turns out, the notion of globally hyperbolic space-times is essential in the formulation of the initial value problem of general relativity (see Section 1.4).

1.3 Congruences

A significant part of the thesis is concerned with numerical finding of *apparent horizons* (see Section 2.1) which are closely related to the behaviour of null geodesics, and thus it is appropriate to introduce the concepts of expansion, shear and twist of a congruence before proceeding any further.

Assume an open subset O of a manifold M . A *congruence in O* is then a family of curves such that through each point $p \in O$ there passes precisely one curve from this family (Wald, 1984). Apparently, the curves in a congruence do not intersect and can be pictured as a tight bundle of wires. Thus, every congruence defines a (tangent) vector field and conversely, every continuous vector field defines a congruence by means of its integral curves. We shall further restrict our attention to geodesic congruences (each curve in the family is a geodesic). Let us first investigate the case of time-like geodesic congruences and later generalize the obtained results to the less intuitive null case.

Consider now a subfamily of a smooth congruence of time-like geodesics parametrized by their proper time. That is, assume a smooth map $(\tau, s) \rightarrow \gamma_s(\tau)$ (where for each s , the curve $\gamma_s(\tau)$ is a time-like geodesic) which is one-to-one and has smooth inverse. There are two vector fields associated with this map – namely the tangent vector field to the congruence ξ^a for which it holds $\xi^a \xi_a = -1$ and $\xi^a \nabla_a \xi^b = 0$ and the *deviation vector field* η^a which corresponds to the tangent vector field to the curves $\gamma_s(\tau)|_{\tau=\text{const}}$ and represents the displacement to a nearby geodesic. Furthermore, the deviation vector field can be chosen in such a way that it holds $\eta^a \xi_a = 0$ and $\mathcal{L}_\xi \eta^a = 0$ everywhere. Note that the latter condition implies

$$\xi^b \nabla_b \eta^a = \eta^b \nabla_b \xi^a \equiv B^a{}_b \eta^b. \quad (1.10)$$

The tensor field $B_{ab} = g_{ac} B^c{}_b$ satisfies $B_{ab} \xi^b = B_{ab} \xi^a = 0$ (we say that B_{ab} is purely “spatial”) and equation (1.10) allows to interpret it as a measure of failure of η^a to be parallelly transported. Let us further define the tensor field h_{ab} by

$$h_{ab} = g_{ab} + \xi_a \xi_b, \quad (1.11)$$

which in turn defines a three-dimensional spatial metric in the sense that h_b^a is the projection operator into the subspace of the tangent space that is orthogonal to ξ^a . The tensor field B_{ab} can be decomposed into the trace, traceless symmetric and antisymmetric part, i.e.

$$B_{ab} = \frac{1}{3} \theta h_{ab} + \sigma_{ab} + \omega_{ab}, \quad (1.12)$$

where

$$\theta = B^a{}_a = B^{ab}h_{ba}, \quad (1.13a)$$

$$\sigma_{ab} = B_{(ab)} - \frac{1}{3}\theta h_{ab}, \quad (1.13b)$$

$$\omega_{ab} = B_{[ab]}. \quad (1.13c)$$

are respectively called the the expansion, the shear and the twist of a congruence. Section 2.2 of Poisson (2004) provides a nice illustration of these quantities on the kinematics of a deformable medium (the interpretation is the same in the case of congruences). Moreover, it can be shown that a congruence is (locally) hypersurface orthogonal if and only if $\omega_{ab} = 0$.

Differentiating $\nabla_b \xi_a$ along ξ^c and using the Ricci identity, one obtains

$$\xi^c \nabla_c B_{ab} = -B^c{}_b B_{ac} + R_{cba}{}^d \xi^c \xi_d. \quad (1.14)$$

Consequently, this relation leads to three “evolution” equations for θ , σ_{ab} and ω_{ab} . Since the expansion is of great importance in the following chapters, we present the evolution equation for θ which can be obtained by taking the trace of (1.14),

$$\frac{d\theta}{d\tau} = \xi^c \nabla_c \theta = -\frac{1}{3}\theta^2 - \sigma_{ab}\sigma^{ab} + \omega_{ab}\omega^{ab} - R_{cd}\xi^c \xi^d, \quad (1.15)$$

which is known as Raychaudhuri’s equation and it is fundamental in proving the singularity theorems (see Chapter 2). The evolution equations for shear and twist can be derived by considering the traceless symmetric and antisymmetric part of equation (1.14).

Let us now turn our attention to the case of null geodesic congruences. Although the situation is analogous to the previous case, there are some differences worth investigating. First of all, each curve is now an affinely parametrized null geodesic which means that the tangent vector field k^a satisfies $k^a k_a = 0$, $k^a \nabla_a k^b = 0$ and $k^a \nabla_b k^a = 0$. Since k^a is now orthogonal to itself, there is no natural way of fixing the scales along different geodesics. We can also introduce an orthogonal deviation vector field η^a , for which it holds $\eta^a k_a = 0$ everywhere. Contrary to the case of time-like geodesic congruences, this condition does not imply that η^a has no component parallel to k^a and therefore some difficulties with isolating the transverse (or spatial) metric are to be expected. Indeed, for time-like geodesics the orthogonality condition implied no component parallel to k^a whereas in the present case these are two independent conditions imposed on the vectors in the tangent space. These vectors then constitute a two-dimensional subspace of the tangent space and it can be shown that, when restricted to this subspace, the metric g_{ab} gives rise to a two-dimensional positively definite transverse metric, although not in a unique way (see Wald, 1984; Poisson, 2004). In order to construct such a transverse metric, assume another null vector field l^a which satisfies $k^a l_a = -1$ everywhere. Consider now the tensor field h_{ab} given by

$$h_{ab} = g_{ab} + k_a l_b + k_b l_a, \quad (1.16)$$

for which it holds

$$h_{ab} k^b = h_{ab} l^b = 0, \quad h_a{}^a = 2, \quad h_c{}^a h_b{}^c = h_b{}^a. \quad (1.17)$$

These conditions imply that h_{ab} is effectively two-dimensional and purely transverse. However, h_{ab} is not uniquely defined as the two conditions, $l^a l_a = 0$ and $l^a k_a = -1$, do not fix the auxiliary null vector field. As anticipated, we shall call such a tensor field (defined by (1.16)) the transverse metric. Note that despite its non-uniqueness, quantities such as the expansion are independent of the choice of the auxiliary field.

Having constructed the transverse metric, we can now proceed as in the case of time-like geodesic congruences. First, we introduce the tensor field B_{ab} (in analogy with (1.10))

$$B_{ab} = \nabla_b k_a, \quad (1.18)$$

which measures the failure of η^a to be parallelly transported. As before, B_{ab} is orthogonal to k^a , but it is *not necessarily* orthogonal to l^a , which means that there is some non-transverse part which needs to be removed. This can be done using the projection operator h_b^a into the orthogonal and transverse subspace to the congruence. Denoting $\hat{B}_{ab} = h_a^c h_b^d B_{cd}$ and $\hat{\eta}^a = h_b^a \eta^b$, the purely transverse equivalent of equation (1.10) for the null case can be shown to hold,

$$h_c^a (k^b \nabla_b \hat{\eta}^c) = \hat{B}_c^a \hat{\eta}^c. \quad (1.19)$$

Analogous to the previous case, we decompose \hat{B}_{ab} into the trace, traceless symmetric and antisymmetric part as follows

$$\hat{B}_{ab} = \frac{1}{2} \theta \hat{h}_{ab} + \sigma_{ab} + \omega_{ab}, \quad (1.20)$$

where the numerical factor $1/2$ is related to the dimension of the transverse metric. Otherwise, the definitions of θ , σ_{ab} and ω_{ab} are equivalent to those stated in (1.13a)–(1.13c). In addition, (1.13a) implies that the expansion can be also calculated as

$$\theta = \nabla_a k^a, \quad (1.21)$$

from which it is obvious that the expansion is independent of the choice of the auxiliary null field. Using the same steps as in the time-like case, we obtain Raychaudhuri's equation for a congruence of null geodesics,

$$\frac{d\theta}{d\lambda} = k^a \nabla_a \theta = -\frac{1}{2} \theta^2 - \sigma_{ab} \sigma^{ab} + \omega_{ab} \omega^{ab} - R_{ab} k^a k^b, \quad (1.22)$$

where λ denotes the affine parameter along the congruence. It should be noted that this equation is, as well as the expansion, invariant under a change of the auxiliary null field.

1.4 Initial value formulation

Exact (analytic) solutions of Einstein's equations constitute only a small fraction of all possible space-times. However, obtaining non-analytical solutions requires to solve the field equations numerically and it is not a priori clear whether general relativity admits a well-posed initial value formulation. It can be shown, though,

that initial value formulation for Einstein's field equations is indeed possible in the sense outlined in this section. More thorough introduction to this issue can be found in Wald (1984) which we closely follow.

First, let us take a closer look at the *3+1 formalism* which is utterly essential for the well-posed initial value formulation (and thus numerical simulations) of general relativity. Let (M, g_{ab}) be a globally hyperbolic space-time. Then it is possible to foliate M into a family of space-like hypersurfaces Σ_t which arise as level sets of a scalar function t that corresponds to a global time. The space-time metric g_{ab} then induces a Riemannian 3-metric h_{ab} on the family of hypersurfaces,

$$h_{ab} = g_{ab} + n_a n_b, \quad (1.23)$$

where n_a is the unit normal vector field to the slices, i.e. $n_a n^a = -1$. For n_a it holds

$$n_a = -N \nabla_a t \quad (1.24)$$

where N is the lapse function defined by

$$g^{ab} \nabla_a t \nabla_b t = -\frac{1}{N^2}. \quad (1.25)$$

Let t^a be the vector field satisfying $t^a \nabla_a t = 1$. For its decomposition into the parallel and orthogonal part with respect to the slices we get

$$t^a = N n^a + N^a, \quad (1.26)$$

where $N^a = h_b^a t^b$ is the shift vector. The field t^a can then be interpreted as the "flow of time" in the following sense: as we advance in the coordinate time t from t_0 to some later time t_1 , we move from the initial slice Σ_{t_0} to Σ_{t_1} . Hence, if we identify the slices using the diffeomorphism induced by the integral curves of t^a , we can view the effect of moving forward in time as a change of the induced metric on the initial slice. Furthermore, we can interpret a globally hyperbolic space-time (M, g_{ab}) as the time development of a Riemannian metric h_{ab} on a fixed three-dimensional space-like hypersurface. This motivates the proposition that appropriate initial data should consist of a Riemannian metric h_{ab} and its time derivative on a three dimensional manifold Σ . The correct notion of time derivative of the induced metric turns out to be the extrinsic curvature K_{ab} defined by

$$K_{ab} = \frac{1}{2} \mathcal{L}_n h_{ab} = \nabla_{(c} n_{d)} h_a^c h_b^d = h_a^c \nabla_c n_b, \quad (1.27)$$

which describes the failure of the unit vector field to be parallelly transported along the hypersurfaces.

Paraphrasing Wald, it can be shown that:

Given appropriate initial data consisting of the triple (Σ, h_{ab}, K_{ab}) subject to certain initial value constraints, there exists a globally hyperbolic space-time (M, g_{ab}) satisfying Einstein's equations which possesses a Cauchy surface diffeomorphic to Σ on which the induced metric is h_{ab} and the extrinsic curvature is K_{ab} . Furthermore, this solution depends continuously on the initial data, satisfies the desired domain of dependence property, and is unique (in a certain sense).

That said, it is desirable to cast Einstein's equations into a more suitable form that reflects the well-posed initial value problem as formulated above. Using the 3+1 formalism, it is possible to project the field equations into directions parallel and orthogonal to the family of slices. That is, if all non-trivial projections using the projection operator h_b^a and the unit vector field n^a are made, a system of nonlinear partial differential equations equivalent to the field equations is obtained. It is also particularly useful to express these projections using quantities intrinsic to the family of hypersurfaces and quantities residing in the orthogonal complement of these hypersurfaces, for instance h_{ab} , K_{ab} or a three-dimensional counterpart of the curvature tensor ${}^{(3)}R_{abcd}$ which is related in the standard way to the unique covariant derivative D_a compatible with the induced metric through the three-dimensional Christoffel symbols ${}^{(3)}\Gamma_{bc}^a$. This significantly simplifies the final system of equations. In addition, it can be proved that D_a is related to the four-dimensional covariant derivative through

$$D_a T^{bc\dots}_{de\dots} = h_a^k h_l^b h_m^c h_d^n h_e^o \dots \nabla_k T^{lm\dots}_{no\dots}, \quad (1.28)$$

where $T^{bc\dots}_{de\dots}$ is a general smooth tensor field on M .

Skipping the derivation, we present the non-trivial projections of the Riemann tensor associated with the four-dimensional metric:

$$R^k{}_{lmn} h_k^a h_b^l h_c^m h_d^n = {}^{(3)}R^a{}_{bcd} + K_c^a K_{bd} - K_d^a K_{bc}, \quad (1.29a)$$

$$R^k{}_{lmn} n_k h_b^l h_c^m h_d^n = D_d K_{bc} - D_c K_{bd}, \quad (1.29b)$$

$$R^k{}_{lmn} n_k h_b^l n^m h_d^n = D_d a_b + a_b a_d + K_{bq} K_d^q - \mathcal{L}_n K_{bd}, \quad (1.29c)$$

where $a_b = n^c \nabla_c n_b$ is the acceleration of normal observers and $\mathcal{L}_n K_{bd}$ is the Lie derivative of the extrinsic curvature tensor along the normal unit vector field n_a . Equations (1.29a), (1.29b) and (1.29c) are known as the Gauss, Codazzi and Ricci equation, respectively. Similarly, it can be shown that the non-trivial projections of the Ricci tensor read

$$R_{kl} h_a^k h_b^l = {}^{(3)}R_{ab} + K K_{ab} - D_b a_a - a_a a_b + h_a^k h_b^l n^c \nabla_c K_{kl}, \quad (1.30a)$$

$$R_{kl} n^k h_b^l = D_c K_b^c - D_b K, \quad (1.30b)$$

$$R_{kl} n^k n^l = \nabla_b a^b - K_c^b K_b^c - n^b \nabla_b K. \quad (1.30c)$$

For the scalar curvature it holds

$$R = {}^{(3)}R + K^2 - K_{ab} K^{ab} - 2R_{ab} n^a n^b. \quad (1.31)$$

Equations (1.29a)–(1.29c) imply the following projections of the field equations:

$$D_b K_a^b - D_a K = 8\pi T_{kl} n^k h_a^l, \quad (1.32a)$$

$${}^{(3)}R + K^2 - K_{ab} K^{ab} = 16\pi T_{ab} n^a n^b + 2\Lambda, \quad (1.32b)$$

$$\begin{aligned} {}^{(3)}R_{ab} + K K_{ab} - D_b a_a - a_a a_b + h_a^k h_b^l n^m D_m K_{kl} &= \\ &= 8\pi T_{kl} h_a^k h_b^l + (\Lambda - 4\pi T) h_{ab}. \end{aligned} \quad (1.32c)$$

Equations (1.32a) and (1.32b) do not involve any second time derivatives of the metric and hence they merely provide constraints on initial data (in analogy with

electromagnetism). These equations are called the momentum and Hamiltonian constraint, respectively. Equation (1.32c) may be further rewritten in the form

$$\mathcal{L}_t K_{ab} = N[D_b a_a + a_a a_b - K K_{ab} + 2K_{ak} K_b^k - {}^{(3)}R_{ab} + 8\pi T_{kl} h_a^k h_b^l + (\Lambda - 4\pi T)h_{ab}] + \mathcal{L}_N K_{ab}, \quad (1.33)$$

which reflects the evolution of initial data along the vector field t^a rather than n^a .

The absence of the second time derivatives in equations (1.32a) and (1.32b) implies the possibility of the whole system being underdetermined. Indeed, it can be demonstrated that the Bianchi identities

$$\nabla_b G^{ab} = 0 \quad (1.34)$$

ensure that the constraints are satisfied at all times provided the spatial components of Einstein's equations are satisfied everywhere and the constraints are satisfied initially. That means that the field equations are equivalent to six evolution equations and four initial value constraints and hence, Einstein's equations form an undetermined system for g_{ab} . However, g_{ab} can be rewritten using the lapse N , the shift N^a and the induced metric h_{ab} . At the beginning of this section we argued that appropriate initial data should consist only of h_{ab} and K_{ab} and not of N , N^a and their "time" derivatives. That is, the shift and the lapse are not considered dynamical variables in the well-posed initial value formulation of general relativity. The reason for this is that they just prescribe how to move forward in time and can be chosen arbitrarily (further motivation can be found in the Hamiltonian formulation of general relativity). If we specify N and N^a , we get a system of six evolution equations for six unknown components of h_{ab} together with four initial value constraints. Not only is this system fully determined but it also reduces the number of independent functions that need to be specified on the initial slice from twelve to eight. In addition, four of these functions are related to the choice of coordinates – it is possible to freely choose the initial space-like slice Σ_{t_0} and specify the spatial coordinates within it. Finally, the four remaining functions correspond to two pairs of independent components of h_{ab} and K_{ab} which represent the two dynamical degrees of freedom characterizing a gravitational field in general relativity.

The fundamental idea of this section may be formulated as a theorem which can be found in Wald (1984):

Let Σ be a three-dimensional C^∞ manifold, let h_{ab} be a smooth Riemannian metric on Σ , and let K_{ab} be a smooth symmetric tensor field on Σ . Suppose h_{ab} and K_{ab} satisfy the constraint equations (1.32a) and (1.32b). Then there exists a unique C^∞ space-time, (M, g_{ab}) , called the maximal Cauchy development of (Σ, h_{ab}, K_{ab}) , satisfying the following four properties:

- (i) (M, g_{ab}) is a solution of Einstein's equations.
- (ii) (M, g_{ab}) is globally hyperbolic with Cauchy surface Σ .
- (iii) The induced metric and extrinsic curvature of Σ are, respectively, h_{ab} and K_{ab} .

- (iv) *Every other space-time satisfying (i)–(iii) can be mapped isometrically into a subset of (M, g_{ab}) . Furthermore, (M, g_{ab}) satisfies the desired domain of dependence property in the following sense. Suppose (Σ, h_{ab}, K_{ab}) and $(\Sigma', h'_{ab}, K'_{ab})$ are initial data sets with maximal developments (M, g_{ab}) and (M', g'_{ab}) . Suppose there is a diffeomorphism between $S \subset \Sigma$ and $S' \subset \Sigma'$ which carries (h_{ab}, K_{ab}) on S into (h'_{ab}, K'_{ab}) on S' . Then $D(S)$ in the space-time (M, g_{ab}) is isometric to $D(S')$ in the space-time (M', g'_{ab}) . Finally, the solution g_{ab} on M depends continuously on the initial data (h_{ab}, K_{ab}) on Σ .*

1.5 Conformal transformations

When solving Einstein's equations using the formalism of the previous section, specification of initial data on a space-like hypersurface Σ in the form of a Riemannian metric h_{ab} and a symmetric tensor K_{ab} is required. Initial data cannot be arbitrary, however, but they have to conform to the constraint equations (1.32a) and (1.32b). Constructing initial data therefore requires solving these constraints with appropriate boundary and initial conditions corresponding to the problem. Fortunately, this process can be significantly simplified utilizing *conformal transformations* of the three-dimensional spatial metric h_{ab} (as opposed to conformal transformations of the space-time metric g_{ab}). We summarize here basic principles of this technique; more details together with derivations can be found in Chapter 3 of Baumgarte and Shapiro (2010).

Let ψ be a smooth positive function. The conformally related metric \bar{h}_{ab} to the spatial metric h_{ab} is then defined by

$$h_{ab} = \psi^4 \bar{h}_{ab}. \quad (1.35)$$

Note that conformal transformations are not, in general, associated with a diffeomorphism. We shall denote \bar{D}_a the covariant derivative and $\bar{\Gamma}_{bc}^a$ the Christoffel symbols compatible with the conformally related metric. Under a conformal transformation, the scalar curvature transforms as

$${}^{(3)}R = {}^{(3)}\bar{R}\psi^{-4} - 8\psi^{-5}\bar{D}^2\psi, \quad (1.36)$$

where $\bar{D}^2 = \bar{h}^{ab}\bar{D}_a\bar{D}_b$ denotes the covariant Laplace operator. Similarly, the Hamiltonian constraint (1.32b) now reads

$$8\bar{D}^2\psi - {}^{(3)}\bar{R}\psi - \psi^5 K^2 + \psi^5 K_{ab}K^{ab} = -16\pi\psi^5 T_{ab}n^a n^b, \quad (1.37)$$

where the cosmological constant is set to zero. In general, the extrinsic curvature K_{ab} has to satisfy the momentum constraint (1.32a) as well. Nevertheless, we are mostly interested in the case of an (electro)-vacuum space-times that possess a time-symmetric initial space-like hypersurface, and for such space-times, the momentum constraint is almost automatically satisfied. Indeed, the extrinsic curvature on a time-symmetric slice is identically zero (this can be considered to be our working definition of a time-symmetric hypersurface) and for vacuum

space-times the constraint equations reduce to one equation for the conformal factor (provided that the conformally related metric is specified),

$$8\bar{D}^2\psi - {}^{(3)}\bar{R}\psi = 0. \quad (1.38)$$

On the other hand, electro-vacuum space-times lead to the set of two equations

$$T_{kl}n^k\bar{h}^{la} = 0, \quad (1.39a)$$

$$8\bar{D}^2\psi - {}^{(3)}\bar{R}\psi = -16\pi\psi^5 T_{kl}n^kn^l, \quad (1.39b)$$

where $T_{ab} = \frac{1}{4\pi}[F_{ak}F_b{}^k - \frac{1}{4}\eta_{ab}F_{kl}F^{kl}]$ is the energy-momentum tensor of electromagnetic field. These equations have to be supplemented by Maxwell's equations

$$\nabla_k F^{ak} = 0, \quad (1.40a)$$

$$\nabla_{[c}F_{ab]cykl} = 0. \quad (1.40b)$$

For given components of the conformally related metric, equation (1.39a) imposes certain conditions on electromagnetic field (for conformally flat spatial metrics it implies vanishing of the Poynting vector) while equation (1.39b) can be viewed as an equation for the conformal factor.

Let us devote the rest of the section to the case of a vacuum space-time possessing time-symmetry. Let us further assume the conformally related metric to be flat, that is $\bar{h}_{ab} = \delta_{ab}$. In such a case, we call the physical spatial metric h_{ab} conformally flat. This assumption considerably simplifies equation (1.38) since \bar{D}_a becomes the flat covariant derivative, or partial derivative in Cartesian coordinates. On top of that, the scalar curvature of the conformally related metric vanishes identically. Equation (1.38) then reduces to the Laplace equation for the conformal factor,

$$\bar{D}^2\psi \equiv \Delta\psi = 0. \quad (1.41)$$

Note that suitable boundary conditions must be specified for ψ to be unique as a solution of the Laplace equation. Assuming spherical symmetry and asymptotical flatness of the physical spatial metric, we obtain

$$\psi = 1 + \frac{M}{2r}. \quad (1.42)$$

where we adopted spherical coordinates. It is trivial to show that such conformal factor agrees with the spatial part of the Schwarzschild metric in isotropic coordinates, i.e.

$$dl^2 = \left(1 + \frac{M}{2r}\right)^4 [dr^2 + r^2(d\theta^2 + \sin^2\theta d\phi^2)], \quad (1.43)$$

and M corresponds to the mass of a Schwarzschild black hole. This result can be further generalized to the case of multiple black holes initially at rest due to the linearity of equation (1.40b). In such a case though, omitting of higher multipoles cannot be justified by the requirement of spherical symmetry but rather by the

condition on positivity of the conformal factor. Thus, the solution for multiple black holes is simply obtained by adding individual contributions,

$$\psi = 1 + \sum_{i=1}^N \frac{M_i}{2r_i}, \quad (1.44)$$

where r_i is the coordinate distance of the i th black hole from the origin of the coordinate system. This statement is not quite correct as $r_i = 0$ corresponds to the other spatial infinity related to the i th black hole rather than its centre (in analogy with the Schwarzschild solution, it can be demonstrated that as r_i tends to zero, we enter a whole new asymptotically flat region related to the i th black hole and connected to the original asymptotically flat region via the Einstein–Rosen bridge). Nevertheless, this labeling of individual black holes is unique and therefore justified.

This example nicely illustrates that once the necessary formalism is set up, the process of obtaining a solution to Einstein’s equations corresponding to suitable initial data can become almost trivial, which reflects how powerful the technique of conformal transformations actually is.

2. Black holes and singularities

Black hole space-times, characterized by the existence of the black hole region from which not even light can escape, represent the most fascinating and thought-provoking solutions to Einstein's field equations. To gain an insight into this issue, let us define the notions related to such space-times in a more precise manner. Namely (see Poisson, 2004):

The black hole region B of a space-time manifold M is the set of all events that do not belong to the causal past of the future null infinity \mathcal{I}^+ , i.e.

$$B = M \setminus J^-(\mathcal{I}^+).$$

Loosely speaking, \mathcal{I}^+ contains the future endpoints of all “outgoing” null geodesics. Consequently, *the event horizon H is defined to be the boundary of the black hole region:*

$$H = \partial B = \partial(J^-(\mathcal{I}^+)).$$

The event horizon of a black hole is a one-way membrane generated by outward-going future-directed null geodesics that never reach infinity but neither fall into the black hole. A general space-time containing a black hole then consists of two causally disconnected regions separated by the event horizon.

Black holes are closely related to the concept of singularities which are intuitively understood as locations at which the metric behaves in some pathological way (e.g. the curvature tends to infinity when these locations are approached). The Schwarzschild solution along with the FLRW metric serve as the prime examples of this behaviour. However, not all such pathological locations correspond to a real physical singularity since the problems with the metric can be caused merely by the choice of an inappropriate coordinate system – again as in the case of the Schwarzschild solution. In addition, precise definition of a singularity turns out to be quite problematic, as the intuitive notion of points where the curvature blows-up does not suffice. The most satisfactory approach to this problem seems to be the removal of all such ill-behaved points and to study the effects of these holes on the space-time, as there should exist geodesics which end in these holes (such geodesics are said to be incomplete). Thus, we define a space-time to be singular if it contains at least one incomplete geodesic. Nevertheless, this definition also leads to singular space-times which do not correspond to the intuitive notion of excised points (for more details see Wald, 1984).

Still, it might seem that singularities are simply an artifact of highly symmetric exact solutions to Einstein's equations rather than a genuine phenomenon that could, in principle, be observed. This is indeed the case for a collapsing spherical dust shell in classical mechanics which leads to a singularity at $r = 0$. However, any perturbations from the spherical case give no singularities and therefore, they are not expected to actually form during collapse in this context. On the other hand, the singularity theorems of general relativity ensure that singularities indeed *do* form during collapse of matter, even in a nonspherical case. Furthermore, they prove that singularities (in the sense of the geodesic incompleteness) are true

features of general relativity, not constrained to unrealistically symmetric exact solutions to the field equations. However, it is widely believed that singularities emergent during collapse of matter are contained within the event horizon rather than being naked and so a black hole is formed (c.f. Wald, 1984). If that were not the case, singularities could communicate with their neighbourhood, but since general relativity breaks down at such points, a space-time containing naked singularities would not be fully deterministic. Nonetheless, a singular space-time could accommodate a primordial singularity that is not an outcome of a matter collapse.

In the rest of this chapter, we try to slightly elaborate on the concept of various horizons surrounding black holes and establish tools needed in order to study more general cases of singular space-times.

2.1 Trapped surfaces and apparent horizons

Event horizons are of great importance in numerical simulations of singular space-times, as the knowledge of their location in the course of a simulation (not just in “post-processing”) is frequently needed in order to exclude the neighbourhood of singularities from the grid so that the simulation is not influenced by these problematic regions. This is allowed since the black-hole interior does not affect the exterior region. However, the global nature of the event horizon makes it difficult to perform real-time localization since the entire future of the simulated space-time is needed in order to decide whether a given region lies within it. In reality though, it is often sufficient to evolve the space-time until a stationary state is reached.

Thus, a more local notion of the horizon at any “given time” is desired. As it turns out, the concept of apparent horizons is exactly what is needed. Contrary to the global nature of the event horizons, apparent horizons are locally defined on each slice and therefore can be localized “on the go” during simulation. Provided certain suitable conditions are satisfied, an apparent horizon (if existent) must always reside within the event horizon and so it is safe to excise its interior from the grid. In order to define an apparent horizon, we must first introduce trapped surfaces (more details can be found in Baumgarte and Shapiro, 2010).

Assume a closed smooth two-dimensional surface S located within a three-dimensional space-like hypersurface Σ which is embedded in a space-time (M, g_{ab}) . Now consider its outward pointing unit normal field s^a . Evidently, s^a satisfies

$$s^a s_a = 1, \quad s^a n_a = 0, \quad (2.1)$$

where n^a is the unit normal vector field to Σ (see Chapter 1). The spatial metric h_{ab} induces the two-dimensional metric m_{ab} on S , similarly as g_{ab} induces the three-dimensional metric h_{ab} on Σ . This metric is given by

$$m_{ab} = h_{ab} - s_a s_b = g_{ab} + n_a n_b - s_a s_b. \quad (2.2)$$

For each point on S there is a pair of future-pointing null geodesics whose projection to Σ is orthogonal to S . These geodesics are given by the tangents

$$k^a = \frac{1}{\sqrt{2}}(n^a + s^a), \quad l^a = \frac{1}{\sqrt{2}}(n^a - s^a). \quad (2.3)$$

We call k^a the *outgoing* null geodesics and l^a the *ingoing* null geodesics and it holds $k^a k_a = l^a l_a = m_{ab} k^a = m_{ab} l^a = 0$, $k^a l_a = -1$. Expansion θ of the outgoing null geodesic congruence is then

$$\theta = \nabla_a k^a = m^{ab} \nabla_a k_b. \quad (2.4)$$

Expansion of the ingoing null geodesic congruence is defined analogically. We define a *trapped surface* as a closed smooth two-dimensional surface embedded in Σ , whose expansion of both the ingoing and outgoing null geodesics is everywhere negative. In the definition of an *outer-trapped surface*, only the expansion of the outgoing null geodesics is required to be negative. A trapped region is then any region in Σ which contains outer-trapped surfaces. Finally, we define a *marginally outer-trapped surface* (MOTS) as the outer boundary of any connected trapped region. On any MOTS, the expansion of the outgoing null geodesics is zero (for proof see Hawking and Ellis, 1994). If a given MOTS is not contained in any other MOTS, it is known as an *apparent horizon* (Thornburg, 2006). Despite this slight difference in terminology (any apparent horizon is a MOTS but only the outermost MOTS is an apparent horizon), both an apparent horizon and a MOTS share the same properties and the defining equation

$$\sqrt{2}\theta = D_a s^a + K - s^a s^b K_{ab} = 0, \quad (2.5)$$

where $K = K^a_a$. As mentioned at the beginning of this section, it can be shown that, under certain conditions, the existence of an apparent horizon implies the existence of the event horizon that contains the apparent horizon, or at worst coincides with it. However, the opposite implication does not hold – the absence of an apparent horizon in a given space-like slice does not imply that there is no black hole, i.e. the existence of an apparent horizon is slicing-dependent as opposed to slicing-independence of the event horizon. In addition, for stationary space-times the event and apparent horizon always coincide and therefore it is expected that an apparent horizon closely approximates the event horizon in the case of space-times approaching their stationary final state (see Hawking and Ellis, 1994).

2.2 Uniqueness theorems and topology of horizons

If we admit the existence of singularities and black holes associated with them, there arises a natural question of uniqueness of space-times containing these phenomena (at least under certain simplifying criteria). For (electro-)vacuum space-times, there exists a collection of elegant theorems which try to answer

this. In the following paragraphs, we present a brief and concise summary of these theorems (we closely follow Poisson’s introduction to the properties of general black holes).

The first theorem proved by Israel (1967) states that *if a black hole in a vacuum asymptotically flat space-time is static, then it must be spherically symmetric and it is described by the Schwarzschild solution*. Already before Israel managed to show the validity of this statement, it was known that the vacuum space-time corresponding to the exterior of a spherically symmetric body of mass M is uniquely determined by the Schwarzschild solution and is therefore static (under the assumption of the Schwarzschild radius being smaller than the radius of the body). This statement is known as Birkhoff’s theorem. Furthermore, Israel’s theorem can be shown to imply that complete gravitational collapse results in a Schwarzschild black hole independently of the initial shape of the collapsing body in the case of null angular momentum (all higher multipoles are radiated either to infinity or into the black hole during collapse). Next, if a static black hole carries an electric charge, then a generalization of Israel’s theorem takes place and the black hole must be of the Reissner–Nordström type (Israel, 1968).

If a black hole is axially symmetric then an extension of Israel’s theorem holds as established by Carter (1971) and Robinson (1975). This theorem states that an isolated stationary axially symmetric black hole must be of the Kerr type. Furthermore, if we admit that such a black hole carries electric charge as well, then it must be a Kerr–Newman black hole (Mazur, 1982). On top of that, Hawking showed that if a black hole is stationary then it is either static or axially symmetric. That means that the space-time corresponding to a rotating stationary black hole is automatically axially symmetric (Hawking, 1972).

In conclusion, isolated black holes in (electro-)vacuum space-times are subject to the uniqueness theorems as summarized above. These theorems associate spherical and axial symmetry to staticity and stacionarity of the space-time under consideration. Consequently, any isolated stationary black hole in an asymptotically flat space-time is uniquely characterized by three parameters: mass, charge and angular momentum. Furthermore, the uniqueness theorems imply that the event horizon of any such black hole has the topology of a sphere. Note that in the stationary case the event horizon coincides with an apparent horizon and therefore it also assumes spherical topology. Thus, provided we do not want to loosen the reasonable requirements of asymptotical flatness and electro-vacuum character of a space-time, it seems that the condition of stationarity needs to be abandoned in order to investigate topologies other than spherical.

3. Brill–Lindquist initial data

In Chapter 1, we revised the initial-value formulation of general relativity and showed advantages of the conformal-transformation technique when constructing initial data using the example of a system of multiple uncharged black holes initially at rest. Now, it is time to generalize these results to obtain initial data corresponding to a time-symmetric hypersurface accommodating a system of *charged* black holes initially at rest. Such a system was discussed for the first time by Brill and Lindquist (1963), which motivates the title of this chapter. The subsequent paragraphs outline the basic results derived in this article.

The complete system of Einstein’s and Maxwell’s equations determines the geometry of a space-time manifold and prescribes an antisymmetric tensor field corresponding to the electromagnetic field tensor in it. However, it does not say anything about topology of the manifold. As it turns out, the system admits a spectrum of physically interesting solutions possessing sufficiently general topologies (the well-known examples being the Schwarzschild and Reissner–Nordström solutions corresponding to spherically symmetric space-times carrying mass and charge), a number of them being multiply connected.

Maximal analytic extensions of these solutions viewed “at an instant of time” can be represented by isometric embedding in three-dimensional Euclidean space with the standard metric. This embedding corresponds to the Einstein–Rosen bridge with topology and curvature illustrated in figure 3.1 and may be considered as a “model” for free mass and charge (a single point charge with mass in an otherwise empty universe).

For modelling interactions between these “particles”, it is necessary to numerically evolve space-times containing multiple Einstein–Rosen bridges and for that, construction of appropriate initial data is required. In Section 1.5 we derived initial data for a system of multiple uncharged black holes (or “particles” in our terminology) as an extension of the Schwarzschild solution. To further generalize this result, we have to solve the system of constraint equations (1.39a)–(1.40b) for the spatial metric and electromagnetic field. In general, the constraint equations also depend on the extrinsic curvature. However, we assume time-symmetric initial data, which means that the extrinsic curvature vanishes identically. Conformal flatness of the spatial metric is assumed as well (in analogy with the example in 1.5). If we adopt three-dimensional Cartesian coordinates on the space-like

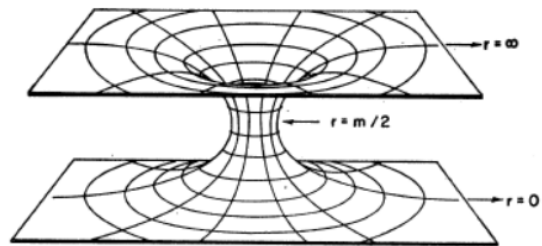


Figure 3.1: Representation of the Einstein–Rosen bridge connecting two asymptotically flat regions of the Schwarzschild/Reissner–Nordström solutions (original picture can be found in Brill and Lindquist, 1963).

hypersurface, equations (1.39a) and (1.39b) reduce to

$$T_{0A}\delta^{AB} = T_{0B} = 0, \quad (3.1a)$$

$$\Delta\Omega = -2\pi\Omega^5 T_{00}, \quad (3.1b)$$

where we denoted the conformal factor by Ω instead of ψ . The first equation is a condition on vanishing of the Poynting vector, while the second equation imposes conditions on the conformal factor. As it turns out, equation (3.1a) is identically satisfied if the only nonzero components of the electromagnetic field tensor correspond to electric field. Therefore, we shall further assume zero magnetic field. For such an electromagnetic field, the constraint equations resulting from equations (1.40a) and (1.40b) take the forms

$$\nabla_A E^A = 0, \quad (3.2a)$$

$$\epsilon_A{}^{BC}\partial_B E_C = 0, \quad (3.2b)$$

where ϵ_{ABC} is the three-dimensional Levi-Civita symbol. Now, suppose the spatial metric and electric field have the simple forms

$$h_{AB} = (\psi\chi)^2 \delta_{AB}, \quad (3.3)$$

$$E_A = \partial_A \ln \frac{\chi}{\psi}. \quad (3.4)$$

Equations (3.1b) and (3.2a) then lead to

$$\Delta\chi = 0, \quad \Delta\psi = 0. \quad (3.5)$$

To sum up, appropriate initial data for a system of charged black holes initially at rest, for which the spatial metric and electric field take the forms (3.3) and (3.4), have to satisfy conditions listed in (3.5). These conditions are imposed on functions χ and ψ into which the conformal factor is split and they require that both χ and ψ solve the Laplace equation (again, in analogy with the example shown in Section 1.5, where the constraint equations reduce to the Laplace equation for the conformal factor). In addition to these requirements, specification of suitable boundary conditions is necessary as well. If we demand that the conformal factor be everywhere strictly positive then both χ and ψ must be everywhere strictly positive or strictly negative (we choose the former option). Condition on asymptotic flatness further requires that $\chi, \psi \rightarrow 1$ as $r \rightarrow +\infty$, where we adopted spherical coordinates. Let us denote these conditions by (i) and (ii), respectively. General solutions satisfying these conditions are given by

$$\chi = 1 + \sum_{i=1}^N \frac{\alpha_i}{r_i}, \quad \psi = 1 + \sum_{i=1}^N \frac{\beta_i}{r_i}, \quad (3.6)$$

where r_i is the coordinate distance of the i th puncture (or deleted point) from the origin of the coordinate system. In accordance with condition (i), it holds $\alpha_i > 0, \beta_i > 0$ for all $1 \leq i \leq N$. The same condition excludes higher multipoles from the solutions.

The three-dimensional line element in spherical (or rather isotropic coordinates) is then given by

$$dl^2 = \left(1 + \sum_{i=1}^N \frac{\alpha_i}{r_i}\right)^2 \left(1 + \sum_{i=1}^N \frac{\beta_i}{r_i}\right)^2 [dr^2 + r^2(\sin^2\theta d\phi^2 + d\theta^2)]. \quad (3.7)$$

Moreover, it can be shown that punctures are not in fact genuine physical singularities but rather correspond to different spatial infinities related to the respective Einstein–Rosen bridges. In this sense, the solution is complete (for more details see the original article by Brill and Lindquist).

At this point, it seems advisable to point out a few properties of the obtained initial data. It should be clear that the spatial metric corresponds to a space with $N + 1$ separate asymptotically flat regions mutually interconnected through Einstein–Rosen bridges. However, one of these regions is special in that all other regions are connected to it (we shall call this region *the upper sheet* and the other regions *the lower sheets*) and that it is not possible to pass from one lower sheet to any other except through the upper sheet (this is evident from the construction of the initial data). Note that solutions containing only one lower sheet connected to the upper sheet via multiple Einstein–Rosen bridges can be constructed as well.

Asymptotic form of the line element (3.7) on each separate lower sheet allows to relate the unknown constants α_i and β_i to the mass of the individual Einstein–Rosen bridges in the following way

$$m_i = \alpha_i + \beta_i + \sum_{i \neq j} \frac{\beta_i \alpha_j + \beta_j \alpha_i}{r_{ij}}, \quad (3.8)$$

where r_{ij} are the coordinate distances between different punctures. The total mass M as measured from the upper sheet is then

$$M = \sum_{i=1}^N \alpha_i + \beta_i. \quad (3.9)$$

Comparison of equations (3.9) and (3.8) shows that the total mass does not simply correspond to the sum of contributions from all “particles”. This is to be expected, since mere adding of the masses does not take into account any interactions between “particles” (it can be shown that the interaction energy is always negative). Furthermore, calculating the flux of electric field on each of the N separate lower sheets relates the unknown coefficients from (3.6) to the charge of the individual “particles” in addition to their mass (for more details see the original paper). This leads to

$$q_i = \beta_i - \alpha_i + \sum_{i \neq j} \frac{\beta_i \alpha_j - \beta_j \alpha_i}{r_{ij}}. \quad (3.10)$$

By requiring positivity of α_i and β_i for all i , it is apparent that q_i can never exceed m_i . Furthermore, in contrast with (3.8) and (3.9), the total charge Q , as measured from the flux of electric field on the upper sheet, is given by the sum of the respective charges due to conservation of flux, i.e.

$$Q = \sum_{i=1}^N q_i. \quad (3.11)$$

If we now assume that the system only consists of one “particle”, equations (3.9) and (3.10) reduce to

$$\left. \begin{array}{l} M = \alpha + \beta \\ Q = \beta - \alpha \end{array} \right\} \implies \alpha = \frac{1}{2}(M - Q), \quad \beta = \frac{1}{2}(M + Q). \quad (3.12)$$

The line element (3.7) then becomes

$$dl^2 = \left(1 + \frac{M - Q}{2r}\right)^2 \left(1 + \frac{M + Q}{2r}\right)^2 [dr^2 + r^2(\sin^2 \theta d\phi^2 + d\theta^2)]. \quad (3.13)$$

This line element corresponds to the spatial part of the Reissner–Nordström metric written in isotropic coordinates, which justifies the whole derivation. The original paper further discusses other possible physical interpretations of these initial data (the interpretation in terms of a system of distinct black holes initially at rest is only valid in the case of large separations) and studies the shape of minimal surfaces in two limiting cases of very small and very large distances between a pair of Einstein–Rosen bridges. However, these results are not that essential for the following and therefore we omit them.

Based on the process of constructing initial data containing multiple Einstein–Rosen bridges (i.e. “particles”, or black holes), both charged and uncharged, we attempt in the following section to create a mathematically interesting and physically compelling candidate for a space-time that could, in principle, admit the existence of MOTSs with toroidal topology.

3.1 Brill–Lindquist rings

In Section 2.2 we presented basic results regarding the uniqueness of (electro-) vacuum space-times containing black holes. In a nutshell, these theorems associate certain spatial symmetries to stationarity, or even staticity of a space-time and vice-versa. Consequently, the space-times characterized by such symmetries are uniquely determined by the well-known solutions of Schwarzschild, Reissner–Nordström and Kerr–Newman, which fixes the topology of their event and apparent horizons. We then concluded that in order to investigate (apparent) horizons of a different topology than spherical, it is necessary to release one or more assumptions made in these theorems.

Therefore, using the apparatus developed in Sections 1.4 and 1.5 and results of the last section, we shall try to construct a candidate for an axially symmetric electro-vacuum space-time containing apparent horizons or at least MOTSs with *toroidal* topology. By the uniqueness theorems, the simplest candidates for admitting such surfaces are non-stationary space-times. Moreover, it seems reasonable to expect some sort of a “ring singularity” to be present.

Thus, consider the same set-up as at the beginning of this chapter. That is, assume time-symmetric conformally flat initial data corresponding to a system of charged black holes initially at rest. We know that the spatial line element defined by such initial data is given by (3.7). Let us further assume that the system under consideration consists of N black holes having equal masses and charges. In addition, assume the N black holes to be symmetrically aligned in a circle with radius b . These symmetries imply

$$\left. \begin{array}{l} M = N(\alpha + \beta) \\ Q = N(\beta - \alpha) \end{array} \right\} \implies \alpha = \frac{1}{2N}(M - Q), \quad \beta = \frac{1}{2N}(M + Q). \quad (3.14)$$

For such a system, functions χ and ψ can be written as

$$\chi = 1 + \frac{M - Q}{4\pi} \sum_{i=1}^N \frac{1}{\sqrt{\rho^2 + z^2 + b^2 - 2b\rho \cos(\phi - \phi_i)}} \frac{2\pi}{N}, \quad (3.15a)$$

$$\psi = 1 + \frac{M + Q}{4\pi} \sum_{i=1}^N \frac{1}{\sqrt{\rho^2 + z^2 + b^2 - 2b\rho \cos(\phi - \phi_i)}} \frac{2\pi}{N}, \quad (3.15b)$$

where we adopted cylindrical coordinates (ρ, ϕ, z) (the system of “particles” is located in the $z = 0$ plane). It is important to realise what we precisely mean by aligning the black holes in a circle. As opposed to the intuitive notion, the deleted points, or the punctures representing the “singularities” of our initial data, do not actually correspond to genuine physical singularities (see the discussion at the end of Section 1.5 which also applies in the present case). What is more, the Brill–Lindquist initial data contain no physical singularities at all (in the sense outlined in Chapter 2). Thus, when talking about black holes, “particles”, deleted points or Einstein–Rosen bridges, we simply refer to the individual punctures which identify them in a unique way. In this sense, aligning the black holes really means aligning the corresponding punctures. Indeed, equations (3.15a) and (3.15b) are obtained by such an alignment of “spatial infinities”.

Consider now the limit in which we send the number of such symmetrically aligned black holes to infinity but simultaneously keep the total mass and charge constant. The sums in (3.15a) and (3.15b) then become integrals with respect to ϕ' , which denotes the angular position of the individual infinitesimal black holes on the ring. We can write

$$\begin{aligned} \chi &= 1 + \frac{M - Q}{4\pi} \int_0^{2\pi} \frac{1}{\sqrt{\rho^2 + z^2 + b^2 - 2b\rho \cos(\phi - \phi')}} d\phi' \\ &= 1 + \frac{M - Q}{2\pi} \left[\frac{K\left(-\frac{4\rho b}{z^2 + (\rho - b)^2}\right)}{\sqrt{z^2 + (\rho - b)^2}} + \frac{K\left(\frac{4\rho b}{z^2 + (\rho + b)^2}\right)}{\sqrt{z^2 + (\rho + b)^2}} \right], \end{aligned} \quad (3.16a)$$

$$\begin{aligned} \psi &= 1 + \frac{M + Q}{4\pi} \int_0^{2\pi} \frac{1}{\sqrt{\rho^2 + z^2 + b^2 - 2b\rho \cos(\phi - \phi')}} d\phi' \\ &= 1 + \frac{M + Q}{2\pi} \left[\frac{K\left(-\frac{4\rho b}{z^2 + (\rho - b)^2}\right)}{\sqrt{z^2 + (\rho - b)^2}} + \frac{K\left(\frac{4\rho b}{z^2 + (\rho + b)^2}\right)}{\sqrt{z^2 + (\rho + b)^2}} \right], \end{aligned} \quad (3.16b)$$

where $K(k)$ is the complete elliptic integral of the first kind defined by

$$K(k) = \int_0^{\pi/2} \frac{1}{\sqrt{1 - k \sin^2 \theta}} d\theta. \quad (3.17)$$

As anticipated, the initial data constructed in this way do contain a singular ring in the sense that the spatial metric is not defined on it. However, it is not a priori clear whether this ring corresponds to an actual physical singularity or it is merely a consequence of pathological behaviour of the coordinate system. Nevertheless, it is not reasonable to expect that these initial data are subject to the same interpretation as the Brill–Lindquist initial data for a finite number

of sufficiently separated Einstein–Rosen bridges, and therefore it is possible that these rings are in fact genuine singularities. Indeed, in the chapters to follow, we present a few indications that this is the case. Finally, we shall refer to the initial data containing such rings as *the Brill–Lindquist rings*.

In conclusion, the space-times obtained by evolving the Brill–Lindquist rings represent appropriate candidates for containing toroidal apparent horizons or at least MOTSs. Nevertheless, in order to verify this hypothesis, it is necessary to take use of numerical methods. Therefore, we devote the following chapter to an introduction of elementary numerical techniques for localizing apparent horizons, with emphasis on space-times possessing axial symmetry.

4. Numerical finding of apparent horizons

In Section 2.1 we stressed the importance of apparent horizons in numerical simulations due to their local nature as opposed to the event horizons. During such simulations of black hole space-times, it is often necessary to localize apparent horizons on each space-like slice in order to excise regions containing singularities from the numerical grid since in such regions the simulation might fail to deliver satisfactory results. However, this requires to numerically localize apparent horizons with sufficient precision “on the fly” in a reasonable amount of time (otherwise the simulation would be useless). Thus, in this chapter we present a short review of various methods suitable for such a task (for a much more thorough introduction into this issue see Thornburg (2006)).

4.1 Overview

When localizing apparent horizons on given hypersurfaces, equation (2.5) (which corresponds to a nonlinear first order partial differential equation for the components of the unit normal vector field to a closed smooth two-dimensional surface contained within the given hypersurface) must be repeatedly solved. If we assume a level-set function parametrization of the two-surface under consideration, we can write

$$s_a = \alpha D_a F, \quad (4.1)$$

where F is a smooth function defined on the hypersurface that also satisfies $F = 0$ on the two-surface and α is a normalization factor ensuring that the condition $s^a s_a = 1$ holds. By construction, condition $s^a n_a = 0$ is satisfied automatically. Thus, substituting (4.1) together with the condition on normalization into equation (2.5) reduces the latter to a nonlinear second order partial differential equation for function F , that is

$$\theta(F, \partial_a F, \partial_{ab} F; h_{ab}, \partial_c h_{ab}, K_{ab}) = 0, \quad (4.2)$$

where the semicolon indicates that the equation parametrically depends on the spatial metric, its derivatives and the extrinsic curvature. It should be noted that such a level-set function parametrization is valid for every surface topology. However, it is sometimes convenient to assume that each connected component of an apparent horizon has the topology of a sphere. In such a case, existence of a local coordinate system in which the shape of the surface corresponds to a “Strahlkörper” (literally “ray-body”, or star-shaped region) is also assumed. Considering the “Strahlkörper” assumption, the surface can be parametrized as

$$r = f(\theta, \phi), \quad (4.3)$$

where r denotes the radial coordinate, θ and ϕ denote the angular coordinates in the local coordinate system and the horizon shape function f is a positive

real-valued function defined on the domain of angular coordinates. Apparently, the level-set function corresponding to such a parametrization is far from being uniquely defined. Nevertheless, the simplest and most common choice is

$$F = r - f(\theta, \phi). \quad (4.4)$$

Consequently, equation (4.2) can be rewritten in terms of the local coordinate system in the following manner

$$\theta(f, \partial_A f, \partial_{AB} f; h_{AB}, \partial_C h_{AB}, K_{AB}) = 0, \quad (4.5)$$

where the only nonzero partial derivatives of the horizon shape function are the ones with respect to θ and ϕ .

Most apparent-horizon finders try to solve equation (4.5) for the horizon shape function f or, in the case of a more general topology, equation (4.4) for the level-set function F . Note that numerical algorithms usually do not distinguish between a MOTS and an apparent horizon since they both must solve equation (2.5) (in this sense, the terms MOTS and apparent horizon are interchangeable in this chapter). Furthermore, there are some criteria which ought to be met by all such algorithms designed for localization of apparent horizons. In addition to accuracy and efficiency, robustness in the sense of finding apparent horizons for a wide range of numerically computed slices without extensive tuning of the algorithm parameters is also a desired property. Unfortunately, no algorithm is perfect in all these dimensions as it is often the case that one or two of these properties are gained at the expense of the other. In addition, apparent-horizon finders can be divided into two broad classes of local and global algorithms. Roughly speaking, local algorithms require a “good” initial guess of the position of an apparent horizon while global algorithms converge to an apparent horizon independently of any initial guess (although in practice even global algorithms may fail to converge). Naturally, this is at the expense of their efficiency. Hence, it is apparent that we should always decide on a specific algorithm based on the problem under study, as different problems require different approach. If we want to track the time evolution of an existing apparent horizon on a family of successive hypersurfaces (which served as our motivation at the beginning of this chapter), local algorithms represent the best choice since we have an excellent initial guess at our disposal in the form of the location of the apparent horizon on the preceding hypersurface. On the other hand, if we are interested only in localizing the apparent horizon on a given slice with no intention of evolving the corresponding space-time (which corresponds to the case of the Brill–Lindquist rings), global algorithms should be used, provided we do not have a “good” initial guess at our disposal. In the following section, we present examples of commonly used algorithms from either class.

4.2 Basic algorithms

If a space-time possesses some kind of symmetry, equations (4.2) and (4.5) assume simplified forms, provided an appropriate coordinate system is adopted.

Furthermore, this simplification allows for the use of specially tailored algorithms which utilize the symmetries at hand. In addition, it should also be noted that most algorithms use the Strahlkörper assumption.

In the case of a spherically symmetric space-time, equation (4.5) reduces to a one-dimensional nonlinear algebraic equation for the horizon shape function f ,

$$\theta(f; h_{AB}, \partial_C h_{AB}, K_{AB}) = 0. \quad (4.6)$$

Assuming usual polar-spherical coordinates (r, θ, ϕ) , equation (4.6) becomes

$$\left(\frac{\partial_r h_{\theta\theta}}{h_{\theta\theta} \sqrt{g_{rr}}} - 2 \frac{K_{\theta\theta}}{g_{\theta\theta}} \right) \Big|_{r=f} = 0, \quad (4.7)$$

which can be solved by any of the scalar *root-finding* algorithms.

In an axially symmetric slice, equation (4.5) turns into a nonlinear second order ordinary differential equation (ODE) represented by a two-point boundary value problem, which can be written as

$$\theta(f, \partial_\theta f, \partial_{\theta\theta} f; h_{AB}, \partial_C h_{AB}, K_{AB}) = 0. \quad (4.8)$$

An ODE (or a system of ODEs) is referred to as a two-point boundary value problem, if it is required to satisfy boundary conditions at more than one value of the independent variable. In our case, the conditions are imposed on the smoothness of the surface due to its axial symmetry, i.e. we require that it holds

$$\partial_\theta f = 0 \quad \text{at } \theta = 0 \text{ and } \theta = \theta_{\max}, \quad (4.9)$$

provided θ has the usual polar-spherical topology. In general, the maximal value θ_{\max} refers to π . However, if the space-like slice also possess the reflection symmetry with respect to the plane $\theta = 0$, then it suffices to put $\theta_{\max} = \pi/2$. This is exactly the case of the Brill–Lindquist rings.

As opposed to the initial value problem, there are no general theorems ensuring the existence or uniqueness of a solution to such an ODE. Thus, a common practice is to determine the remaining unknown initial values at one of the points and “shoot” the solution from there using one of the well-known algorithms for numerical integration of initial value problems. Once the other point is reached by such a solution, we check whether the boundary conditions are satisfied there. If so, we found a solution (which is almost certainly not the case for an arbitrary choice of the remaining initial values at the first point), otherwise an adjustment of the initial data is necessary. In general, the problem reduces to multidimensional root-finding, provided an appropriate function assigning values to our initial guesses is defined in such a manner that it returns zero if all boundary conditions at the other point are met. This whole process is then collectively referred to as *the shooting algorithm*. In addition, equation (4.9) further simplifies things since there is only one initial value parameter to be adjusted and therefore the problem actually reduces to nothing more than scalar root-finding of an appropriately defined function.

Nevertheless, these methods are not applicable to the case of generic slices without any symmetry. Hence, the use of more general algorithms is necessary in order to localize apparent horizons in these hypersurfaces. Below, we present a few examples of such algorithms, each with a brief description (a much more thorough introduction into the issue of general-shape apparent-horizon finders can be found in Thornburg, 2006, which we summarize here in a highly concise manner):

Minimization algorithms

If we define a norm $\| \cdot \|$ on the space of trial surfaces in such a way that it returns zero if and only if the expansion of the trial surface is zero, the problem of finding apparent horizons then reduces to minimization of this scalar function, for which a number of well-known algorithms can be used. An example of such a norm is

$$\| f \| = \int \theta^2 d\Omega, \quad (4.10)$$

where the integral is over all solid angles on the trial surface f . Clearly, the global minima (there can be more MOTSs) of this norm correspond to trial surfaces for which the expansion vanishes. Assuming the Strahlkörper parametrization, individual trial surfaces may be expanded in spherical harmonics, i.e. $f(\theta, \phi) = \sum_{l,m} a_{lm} Y_{lm}(\theta, \phi)$. If we only keep harmonics up to some maximal degree, the minimization process can be performed on the space of their coefficients up to the given degree. However, there are two considerable disadvantages associated with this method. Apart from being relatively slow, minimization algorithms are prone to localizing spurious local minima rather than the global minima corresponding to MOTSs.

Elliptic-PDE algorithms

In the case of a general non-symmetrical space-like hypersurface, the apparent horizon equation (4.5) corresponds to a nonlinear elliptic PDE for the horizon shape function f on the space of angular coordinates, and thus it can be solved using standard finite difference methods, such as Newton’s method.

Horizon pretracking

Horizon pretracking algorithms solve a slightly more general problem than apparent-horizon localization. Their objective is to determine the smallest possible value $E \geq 0$, such that the equation $\theta(f) = E$ has a solution. By monitoring the “time” evolution of the corresponding solutions on each space-like slice, we are able to predict where a new MOTS will appear in a numerical simulation. However, these algorithms tend to be very time consuming.

Flow algorithms

As the only truly global algorithms, they find MOTS by starting with a large trial surface (larger than any possible MOTS), which is then being gradually shrunk inwards in such a way that the surface stops shrinking when it coincides with a MOTS. This is done at the cost of their very slow convergence.

There is one more method worth mentioning which does not really fall into any of the discussed classes. This method turns out to be incredibly useful to the case of the Brill–Lindquist rings, but is otherwise of little importance due to its severely restricted applicability only to time- and axially symmetric slices. Thus,

apart from trivial cases of stationary space-times, it is otherwise not possible to track the evolution of an apparent horizon during a simulation using this method, since an initially time-symmetric slice need not stay that way in “the future”. We present basic characteristics of this method in the following section.

4.3 Method of geodesics

Assume time-symmetric initial data, i.e. assume a three-dimensional space-like hypersurface Σ with a Riemannian metric h_{ab} and vanishing extrinsic curvature, $K_{ab} = 0$. In such a case, the apparent horizon equation in its general form (that is, without any assumptions about the topology of the connected components of the apparent horizon or MOTSs) reduces to

$$D_a s^a = 0, \quad (4.11)$$

which is the condition on vanishing of *the mean curvature*. Thus, for time-symmetric initial data, every solution to equations (4.2), (4.5), or (4.11), respectively, corresponds to a *minimal surface* (see Section 2.1 of Lages, 2010, which we closely follow in the subsequent paragraphs).

Let us further assume conformal flatness of the initial data and let Ω denote the conformal factor. If the space-like hypersurface possesses axial symmetry as well, then the three-dimensional spatial metric defines the line element

$$dl^2 = \Omega^4(d\rho^2 + \rho^2 d\phi^2 + dz^2), \quad (4.12)$$

where we adopted cylindrical coordinates in such a way that $\Omega = \Omega(\rho, z)$. Moreover, due to rotational symmetry, it is possible to completely describe any closed axially symmetric surface using only the curve corresponding to its cross-section along any plane of constant ϕ (we shall denote this curve as γ). Apparently, γ admits any shape as long as the corresponding surface is closed and smooth. Thus, the area A of an arbitrary axially symmetric surface embedded in Σ can be calculated as

$$A = 2\pi \int_{\lambda=0}^{\lambda_1} \rho \Omega^4 \sqrt{\dot{\rho}^2 + \dot{z}^2} d\lambda. \quad (4.13)$$

The dot above ρ and z denotes the derivative with respect to λ . Note that the end value λ_1 is not a priori known. Equivalently, evaluation of the integral in equation (4.13) amounts to calculating the length of γ in the metric given by the two-dimensional line element

$$dl^2 = (\rho \Omega^4)^2(d\rho^2 + dz^2). \quad (4.14)$$

Equations (4.13) and (4.14) further imply that the whole problem of localizing apparent horizons in a time-symmetric conformally flat space-like hypersurface with axial symmetry reduces to finding non-trivial smooth curves with minimal length that define closed surfaces under rotation around the axis of symmetry (we emphasize that the length of these curves is calculated using the line element (4.14) as opposed to (4.12)). The corresponding surfaces then represent the solutions to the original problem, i.e. MOTSs or apparent horizons.

The task of finding curves with minimal length that connect two fixed points leads to a variational problem which in turn leads to a system of second order ODEs known as the geodesic equation. Considering the line element given by (4.14), the geodesic equation assumes the form (as can be found in Lages, 2010)

$$0 = \ddot{\rho} + 8\frac{\partial_z\Omega}{\Omega}\dot{z}\dot{\rho} + \left(\frac{1}{\rho} + 4\frac{\partial_\rho\Omega}{\Omega}\right)(\dot{\rho}^2 - \dot{z}^2), \quad (4.15a)$$

$$0 = \ddot{z} + 4\frac{\partial_z\Omega}{\Omega}(\dot{z}^2 - \dot{\rho}^2) + 2\left(\frac{1}{\rho} + 4\frac{\partial_\rho\Omega}{\Omega}\right)\dot{\rho}\dot{z}. \quad (4.15b)$$

These equations are valid under the assumption of an affine parametrization. Unfortunately, in a general axially symmetric case, solutions to the geodesic equation are not determined uniquely since the only conditions imposed on the shape of the surface are those regarding its smoothness (recall that we completely abandoned the Strahlkörper assumption at the beginning of this section). That is, we only require that all MOTSs with spherical topology cross the z -axis perpendicularly or, in the case of toroidal MOTSs, that they cross the equatorial plane perpendicularly, if we also assume reflection symmetry. Not only do these conditions not determine a unique solution to the geodesic equation, they even lead to a two-point boundary value problem rather than a simpler initial value problem (for which there are general theorems concerning the existence and uniqueness of its solutions). Assuming the reflection symmetry with respect to the equatorial plane, the conditions implied by the smoothness of the surface can be stated as

$$\begin{aligned} \rho(0) &= 0, & \dot{z}(0) &= 0, \\ z(\lambda_1) &= 0, & \dot{\rho}(\lambda_1) &= 0, \end{aligned} \quad (4.16)$$

or

$$\begin{aligned} z(0) &= 0, & \dot{\rho}(0) &= 0, \\ z(\lambda_1) &= 0, & \dot{\rho}(\lambda_1) &= 0, \end{aligned} \quad (4.17)$$

for MOTSs with spherical and toroidal topology, respectively. Note that we completely omitted the case of toroidal MOTSs which do not intersect the equatorial plane.

In conclusion, we managed to reformulate the original problem of solving equation (4.11) to the problem of finding closed smooth surfaces with minimal area. This in turn lead to the geodesic equation ((4.15a) and (4.15b)), implied by the line element (4.14) for the curve corresponding to the cross-section of the minimal surface along any plane of constant ϕ . All solutions to this system must satisfy conditions (4.16) or (4.17), based on the topology of the individual MOTSs, provided the slice possesses additional reflection symmetry. Such a system is not fully determined and leads to a two-point boundary value problem, but can be solved by the shooting algorithm. We shall refer to this reformulation as *the method of geodesics*.

Let us further point out some of the differences between the method of geodesics and the “general” method for axially symmetric slices mentioned in Section 4.2. The latter is more general in the sense that it does not require time-symmetry of the slice in order to be applicable, yet it relies on the rather restricting

Strahlkörper assumption (hence the quotation marks around “general”). On the other hand, the method of geodesics admits any shape of apparent horizons, and thus is favourable in the search of MOTSs with toroidal topology. Nevertheless, both methods lead to a two-point boundary value problem which is solved using the shooting algorithm. Still, it is important to realize that the shooting algorithm is used to determine the appropriate geodesic (or geodesics) in the method of geodesics, while in the “general” method it is supposed to localize individual MOTSs in terms of their horizon shape function. However, both the geodesics and the horizon shape functions must satisfy the boundary conditions implied by the smoothness of an apparent horizon. Ultimately, the two methods should yield the same results in the case of MOTSs with spherical topology.

Now, let us focus our attention on the system of nonlinear ODEs given by (4.15a) and (4.15b). It is apparent that these equations are singular at $\rho = 0$. In order to get rid of this singular behaviour, it is necessary to adopt a better suited set of coordinates. In what follows, we outline the technique introduced in Lages (2010).

First, consider the condition on a geodesic to be affinely parametrized. This can be written as

$$1 = (\rho\Omega^4)^2(\dot{\rho}^2 + \dot{z}^2). \quad (4.18)$$

Since the geodesic equation is a system of second order ODEs, equation (4.18) can be viewed as some kind of a constraint on initial data which need to be specified, so that we obtain a unique solution. Furthermore, it is clear that the constraint (4.18) is satisfied along any geodesic as long as it solves equations (4.15a) and (4.15b) and the initial data satisfy the constraint initially. In addition, equation (4.18) allows us to write $\dot{\rho}$ and \dot{z} as

$$\dot{\rho} = \frac{1}{\rho\Omega^4} \sin \alpha, \quad (4.19a)$$

$$\dot{z} = \frac{1}{\rho\Omega^4} \cos \alpha, \quad (4.19b)$$

where the parameter $\alpha = \arctan(\dot{\rho}/\dot{z})$ corresponds to the orientation of the tangent to a geodesic. The geodesic equation can then be rewritten in terms of ρ , z and α . Let us further introduce new coordinates y_0 , y_1 and y_2 by rescaling these variables, namely

$$\begin{aligned} y_0 &= \rho^2, & \rho &= \sqrt{y_0}, \\ y_1 &= z\rho^2, & z &= y_1/y_0, \\ y_2 &= \alpha\rho^2, & \alpha &= y_2/y_0. \end{aligned} \quad (4.20)$$

Hence, the geodesic equation can be rewritten as the following system of three ODEs:

$$\dot{y}_0 = 2\Omega^{-4} \sin \alpha, \quad (4.21a)$$

$$\dot{y}_1 = \Omega^{-4}(\rho \cos \alpha + 2z \sin \alpha), \quad (4.21b)$$

$$\dot{y}_2 = \Omega^{-4}(\cos \alpha + 2\alpha \sin \alpha + 4\rho(\partial_\rho \Omega \cos \alpha - \partial_z \Omega \sin \alpha)/\Omega), \quad (4.21c)$$

where ρ, z, α and Ω should be understood as functions of y_0, y_1 and y_2 . The boundary conditions implied by (4.16) and (4.17), respectively, take the forms

$$\begin{aligned} y_0(0) = 0, & & y_2(0)/y_0(0) = \pi/2, \\ y_1(\lambda_1)/y_0(\lambda_1) = 0, & & y_2(\lambda_1)/y_0(\lambda_1) = \pi, \end{aligned} \quad (4.22)$$

and

$$\begin{aligned} y_1(0)/y_0(0) = 0, & & y_2(0)/y_0(0) = 0, \\ y_1(\lambda_1)/y_0(\lambda_1) = 0, & & y_2(\lambda_1)/y_0(\lambda_1) = \pm\pi. \end{aligned} \quad (4.23)$$

It is evident that the system of equations (4.21a)–(4.21c) supplemented by the boundary conditions (4.22) is regular at the z -axis as opposed to the original system of ODEs (4.15a) and (4.15b). Note that in the case of toroidal MOTSs, there is not any problem in either of the formulations, since such surfaces do not cross the z -axis at all. Hence, we succeeded in casting the method of geodesics into a form suitable for numerical integration, which will be applied to the case of the Brill–Lindquist rings in the following chapter.

5. Properties of the Brill–Lindquist rings

Finally, we introduced all the necessary tools for investigating the properties of the Brill–Lindquist rings. Most importantly, we derived an especially useful form of the apparent horizon equation (4.21a)–(4.21c), together with the boundary conditions given by (4.22) and (4.23) for MOTSs with spherical and toroidal topology, respectively. Now, we try to localize MOTSs of either topology surrounding these rings.

5.1 Numerical method

The method of geodesics is the algorithm of choice when it comes to numerical finding of MOTSs around the Brill–Lindquist rings, as these hypersurfaces satisfy the rather restrictive conditions for the method’s applicability. Namely, the rings constitute conformally flat time-symmetric initial data possessing the additional axial and reflection symmetry. Thus, it should be clear that assumptions (4.12), (4.16) and (4.17), respectively, were made bearing the specific case of the Brill–Lindquist rings in mind (in principle, the method does not require any of these assumptions to be valid). Although most of the work was already accomplished in Section 4.3, there are still a few things that we need to specify so that the method can be used in numerical computations. Hence, we present a rather detailed description of the three stages of the method’s implementation in the case of the Brill–Lindquist rings in the subsequent paragraphs. Note that this particular implementation which takes the mass, the radius and the charge of the ring as input, was written in Python and therefore it takes advantage of its features as an object-oriented programming language. The final algorithm also heavily relies on the use of functions imported from various libraries. Although we do not present the actual code used in numerical localization of MOTSs, its structure can be partially understood from the description of the individual stages. Nevertheless, where the situation allows it, we try to describe the features of the method in a more general way, so that we can illustrate its application independently of the used programming language or the hypersurface under consideration.

First, consider again the geodesic equation in the form of the system of ODEs (4.21a)–(4.21c). As mentioned before, this system must be solved using the shooting algorithm since there is not a sufficient number of initial conditions for the solution to be uniquely specified. Therefore, in the case of MOTSs with spherical topology, we would like to be able to guess the position of a MOTS at the z -axis, “shoot” the solution from there and then check whether it satisfies the smoothness conditions at the equatorial plane. But, as it turns out, implementing the shooting algorithm is not as straightforward as it may seem. The reason for this is that most standard algorithms for numerical integration of a system of ODEs require initial data to be input in the form of values for the independent variables.

In the case of our system, this would be the triplet $(y_0(0), y_1(0), y_2(0))$. However, if we try to compute the triplet using the boundary conditions supplemented by our initial guess, we get $(y_0(0), y_1(0), y_2(0)) = (0, 0, 0)$. Apparently, this result is obtained for any initial values of z and α at $\rho = 0$. Furthermore, from the numerical point of view, the system is singular for such initial data since it contains division by zero. Nevertheless, the solution to this problem is quite simple. The integration is divided into two phases. First, we hardwire the boundary conditions at the z -axis to the system of ODEs. That is, we substitute the values $\rho = 0, \alpha = \pi/2$ and our initial guess of z into equations (4.21a)–(4.21c) and use any standard numerical integrator supplemented by the zero triplet to compute the values of y_0, y_1 and y_2 at some point near the axis. In our implementation, this is accomplished using the explicit Euler method. In the second phase, the new triplet of values obtained in this way is used as the initial data for, generally, another method of higher order which integrates the original system, since there is no singular behaviour anymore.

To perform this task, we used the function `solve_ivp` imported from **SciPy** which provides a fundamental library for scientific computations. More precisely, we worked with the explicit Runge–Kutta method of order 5(4) which can be specified as one of the parameters of `solve_ivp` (we shall refer to this method as RK45). This method belongs to the family of *adaptive* methods which perform some control over their stepsizes in the course of integration. By adapting the stepsize, it is possible to achieve a certain predetermined accuracy of the obtained solution with minimizing the computational effort. In the case of RK45, this is accomplished by comparing an estimate of the local discretization error (or local truncation error) with the required accuracy at each step. Roughly speaking, the local discretization error approximately corresponds to the difference between solutions calculated using the Runge–Kutta methods of the fifth and fourth order. If the local error is within the required tolerance, we can increase the stepsize in the next integration step. In the opposite case, the stepsize must be adjusted (in the manner prescribed by the asymptotical behaviour of the used methods) and the integration step is computed once again. This is repeated until the required accuracy is achieved. Such methods which compare results obtained by two methods of different orders to adjust their stepsize during integration (and thus speeding up the process) are known as *embedded*. For a much more thorough introduction into the issue of local truncation errors, embedded methods and numerical integration, see Leveque (2007); Press et al. (2007).

Having introduced the basic concepts related to RK45, let us now turn back to the specific case of the Brill–Lindquist rings. When numerically solving the geodesic equation (in the second phase of integration), we required that the local discretization error of the numerical solution be less than $1e-10$. This seems appropriate as we had to resort to numerical methods when evaluating the derivatives of the conformal factor. The differentiation was carried out using the five-point formula which is of the fourth order. Thus, taking the rounding error into account as well, we can reasonably expect the derivatives to be precise only to 10 or 11 decimal places. The stepsize of the explicit Euler method in the first phase was then chosen in such a way that the solution satisfied the accuracy condition, that is we required that the error introduced by this method (which is of the first order)

in one step be less than $1e-10$. Thus, the Euler method operated with a stepsize of the same order as the required accuracy (even though a smaller stepsize might suffice, since if we perform only one step, the method is actually of the second order).

The first stage completes when the solution reaches the desired endpoint and stops. Note that the final value of the affine parameter is not known beforehand and therefore the decision to stop integration is usually controlled by the roots of some *continuous* auxiliary function f that is evaluated at each step (if a root is encountered, integration stops). In practice, the endpoint can be localized only with finite accuracy, since the auxiliary function is evaluated using the numerically obtained solution which is affected by the integration method's error. In general, inaccuracy of the root-finding algorithm used in the process also needs to be taken into account. Thus, the condition on vanishing of the auxiliary function at the endpoint can be satisfied with the accuracy of the numerical-integration method at best. In the case of the Brill–Lindquist rings, integration ends when the numerical solution crosses the equatorial plane since the hypersurface is symmetric with respect to that plane and there is no need to proceed any further (this is valid for MOTSs with both spherical and toroidal topology). Hence, the role of the auxiliary function is assumed by the z coordinate, i.e. $f = y_1/y_0$. Fortunately, it is possible to specify the auxiliary function as one of the parameters of *solve_ivp*. Integration then stops automatically when the endpoint is localized in such a way that the auxiliary function returns zero with the predetermined accuracy of RK45. Lastly, note that the first stage as described above also applies to the case of toroidal MOTSs, except for the first phase of numerical integration since the geodesic equation does not show any singular behaviour when subjected to the toroidal initial conditions.

The second stage defines an appropriate function θ which assigns a certain value to the endpoint of each numerically obtained solution. However, every such solution is uniquely determined by its initial conditions, and therefore the domain of this function can be viewed as the space of the initial data which are not fixed by the boundary conditions. The initial values of z (at the z -axis) and ρ (at the equatorial plane), denoted by z_0 and ρ_0 , represent one-dimensional examples of such spaces in the case of spherical and toroidal MOTSs surrounding the Brill–Lindquist rings. In addition, the values assigned by θ are chosen in such a way that the function measures the “failure” of the boundary conditions to be satisfied at the endpoint. It is a common practice that θ simply assigns to each set of initial data the difference between the required and actual values of the boundary conditions at the endpoint. Apparently, the roots of θ then define the solutions of the original problem (i.e. each root corresponds to a solution which represents a spherical or toroidal MOTS).

This can be nicely illustrated by the example of the Brill–Lindquist rings, where conditions (4.22) and (4.23) imply that an actual solution corresponding to a MOTS should intersect the equatorial plane perpendicularly. That is, we require that it holds $z = 0$ and $\alpha = \pi$, or $\alpha = \pm\pi$ in the case of toroidal MOTSs (based on the position of the endpoint with respect to the starting point). Conveniently, we chose the auxiliary function (which controls the interruption of integration in

the first stage) to correspond to one of the boundary conditions. Hence, within tolerance of the numerical-integration method, $z = 0$ is automatically satisfied. Thus, an appropriate choice of θ in the case of spherical MOTSs seems to be the function which assigns to each z_0 the end value of α (denoted by α_f) shifted by π , i.e.

$$\theta_s(z_0) = \pi - \alpha_f(z_0), \quad (5.1)$$

where the subscript s stands for spherical MOTSs. By the same logic, we define the function θ_t in the following way

$$\theta_t(\rho_0) = \begin{cases} -\pi + \alpha_f(\rho_0) & \text{if } \rho_f > \rho_0 \\ \pi + \alpha_f(\rho_0) & \text{if } \rho_f \leq \rho_0 \end{cases}, \quad (5.2)$$

where ρ_f corresponds to the end value of ρ . Evidently, the roots of θ_s and θ_t identify the solutions in the form of spherical and toroidal MOTSs, respectively. Furthermore, it is clear from definitions (5.1) and (5.2) that these functions measure the deviation from the right angle at which a given solution intersects the equatorial plane. By adopting these definitions of θ_s and θ_t in the search for MOTSs of either topology, the whole problem reduces to mere root-finding (however, it should be noted that there are also alternatives to this technique which lead to minimization process rather than root-finding).

The task of localizing all roots of θ_s within some given interval in a reasonable amount of time constitutes the third stage of our implementation of the method of geodesics. In fact, this stage can be viewed as some sort of a scheme according to which the first two stages are repeated until all the roots within a given interval are found. Nevertheless, the roots of both θ_s and θ_t can only be localized with finite accuracy. In principle, we could demand that the boundary conditions are satisfied within the tolerance of the numerical-integration method (in our case, this would be $1e-10$). In practice, however, no method for numerical integration actually guarantees that the global error does not exceed the prescribed tolerance. Therefore, it is advised to lower the required accuracy of the results at this point as some kind of a safety measure (which also speeds-up the algorithm). Thus, when localizing the roots of θ_s , we requested that the corresponding solutions be precise only to six decimal places (with the last place correctly rounded). However, this is not quite true in the case of toroidal MOTSs, where we actually localized the squares of the roots rather than themselves. Still, the required accuracy should be preserved in most cases even after taking the square root. Lastly, it should be realized that we in fact localize the roots of imprecise representations of θ_s rather than of the precise functions, and thus the actual accuracy of the solutions might be far less than the required six decimal places, depending on the shapes of the examined functions.

Even though there exist global algorithms which, under certain conditions, can localize all the roots of a function in a closed interval, they usually tend to be rather slow. In addition, as it turned out, the structure of functions θ_s and θ_t is not that trivial. In principle, they need not even be continuous, although it is a desired property of a well-posed initial value problem. Fortunately, both functions “almost fulfill” this property; θ_s being continuous in practically all cases and θ_t being piecewise continuous on subintervals in a given interval and separated by “singular gaps” (the character of these singularities will be discussed in

more detail in Sections 5.2 and 5.3, respectively). Note that localizing the roots of a piecewise continuous function is surprisingly demanding, especially when a particular root is situated near some of the points of discontinuity, which happens to be the case for θ_t . Nevertheless, we observed that the “singular gaps” are related to the roots of θ_s in the way discussed in Section 5.3, which allows for isolating these ill-behaved domains with satisfactory precision before making an attempt at finding the roots of θ_t . Note that without this prior isolation of the singular intervals, all the tested root-finding algorithms failed to deliver satisfactory results. Once all the regular subintervals in a given interval have been found, standard root localization is possible. Still, since most global root-finding algorithms accessible in Python’s **scipy.optimize** are vastly time demanding, we had to resort to a more sophisticated method consisting of several steps:

- First, the Python’s library **pychebfun** is used to interpolate θ_t over the individual regular subintervals using the Chebyshev polynomials. The roots of these polynomials then serve as estimates of the actual roots location.
- On the basis of the root estimates, all subintervals on which θ_t changes sign are isolated (note that due to a limited accuracy of the interpolating polynomials, not all approximate roots lie in a distinct sign-changing interval).
- Having localized all such subintervals, any of the local root-finding algorithms (requiring that the function under consideration has opposite signs when evaluated at the bounds of the interval) can be used to localize the actual roots contained within them. In particular, we employed a variation of the classical Brent routine which uses hyperbolic extrapolation instead of inverse quadratic extrapolation. This method can be imported from the already mentioned Python’s **scipy.optimize** library.

It should be noted that since θ_s is generally well-behaved (with occasional difficulties when $z_0 \rightarrow 0^+$), the three steps are also applicable to localization of its roots prior to the isolation of the regular subintervals within θ_t ’s domain.

Before we proceed further, a few more comments regarding the efficiency and accuracy of our implementation of the root-finding algorithm are in order. Mainly, we took advantage of the **multiprocessing** module as a part of **the Python Standard Library** in order to boost the performance of the polynomial interpolation and subsequent approximate-root localization by simultaneously running several separate processes, each for a distinct regular subinterval. The same procedure was used in localization of the actual roots in the individual sign-changing subintervals. Thus, the whole process of root localization was significantly sped up. Moreover, in order to maximize the accuracy of approximate roots and, at the same time, to minimize the time needed for interpolation of the functions, we worked with 40 interpolation points for both θ_s and θ_t . The method then operated with the maximal root resolution of 1/125th of the given interval or, in the case of multiple approximate roots, 1/25th of the minimal distance between them. Naturally, there is generally no guarantee that the interpolation process converges to all the actual roots lying in the interval. Nevertheless, in the case of

smooth non-oscillating functions, this procedure is expected to yield satisfactory results. Based on our experience with θ_t , this conclusion is valid even without assuming non-oscillatory character of the function. What is more, the method proved to reliably localize all the roots of both θ_s and θ_t within regular subintervals of their domains in about two minutes, provided no initial guess of the roots was specified. However, taking use of the secant method, all the roots were found in less than ten seconds if the estimate of their location was sufficiently accurate (this was the situation when tracking the MOTSs of a family of the Brill–Lindquist rings defined by varying one of the input parameter while keeping the rest constant). Finally, we present the obtained results in the following sections.

5.2 Spherical MOTSs

In order to investigate the structure of spherical MOTSs around the Brill–Lindquist rings, we focused on three distinct families of such hypersurfaces. Each family is defined by keeping two of the input parameters constant and varying the third one (the parameters being the radius b , the mass M and the charge Q of the rings). Let us denote these families by $A : (M = 3, Q = 0)$, $B : (b = 1, Q = 0)$ and $C : (b = 1, M = 3)$. For each family, we examined the following properties of spherical MOTSs: the minimal and maximal values of the free parameter for which spherical MOTSs exist; the shape of θ_s for chosen values of the free parameter and the dependence of z_0 corresponding to the individual spherical MOTSs on the free parameter. Note that in our search for spherical MOTSs we restricted the root-finding algorithm only to interval $[0, 3]$ which proved to be satisfactory (in the case of toroidal MOTS, the interval was chosen to be $[0, 2]$). Furthermore, we postpone the depiction of the actual coordinate shapes of the spherical MOTSs to the following section as it is appropriate to visualize the whole system of both the spherical and toroidal MOTSs at once.

Most notably, we observed that in practically all cases spherical MOTSs exist in pairs, with the outer MOTS representing the apparent horizon. That is, for a given combination of the input parameters, there are either no spherical MOTSs or two of them, the only exception being the case of vanishing radius when the Brill–Lindquist ring reduces to a time-symmetric slice of the Reissner–Nordström solution written in isotropic coordinates, and thus only one spherical MOTS exists (see Figure 5.1). This behaviour can be understood from the shapes of θ_s , illustrated in figures 5.2a and 5.2b for the case of families A and B , respectively (qualitatively speaking, family C leads to the same results for increasing charge as family B for decreasing mass, and therefore we omit them). Namely, it seems that for any non-zero radius of the ring, there always exist such values of the mass and charge that θ_s has a negative global minimum accompanied by two roots. If we now consider family A as an example, then by gradually expanding the radius the minimum shifts toward zero until the radius takes the value $b = 1.476110$ (precise to six decimal places, not rounded). For this value, both the spherical MOTSs merge into a single spherical apparent horizon. Furthermore, if we increase the

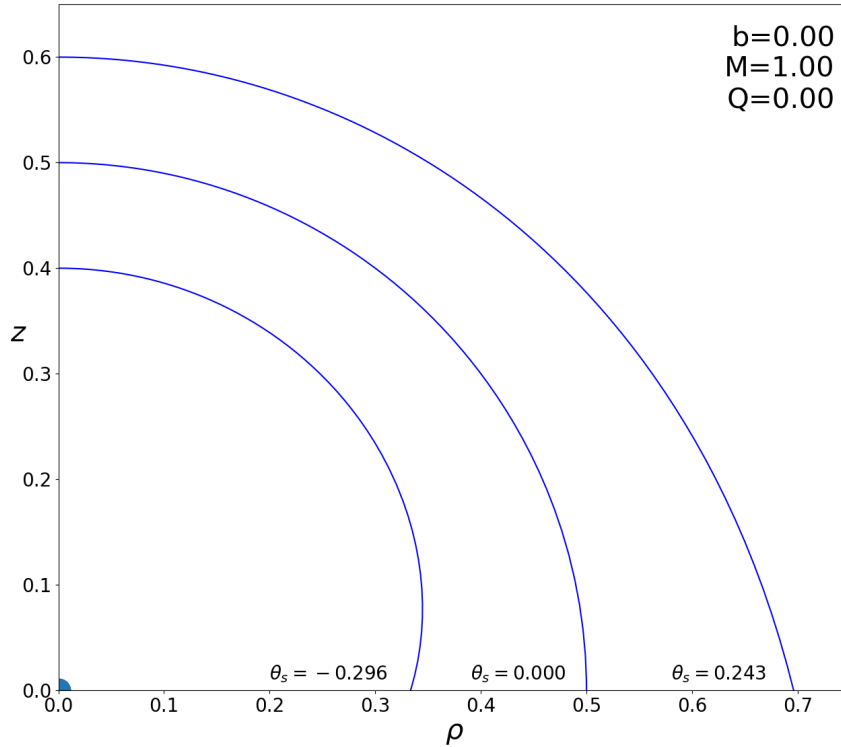


Figure 5.1: Illustration of the shooting algorithm searching for spherical MOTSs in the case of the Brill–Lindquist rings with vanishing radius and charge. As expected, in such a case the problem reduces to the well-known case of a time-symmetric space-like slice of the Schwarzschild solution in isotropic coordinates. Thus, the only spherical MOTS (also corresponding to the apparent horizon) is localized at $z_0 = M/2 = 0.5$.

radius above this value, the global minimum passes zero, and thus θ_s no longer has any roots. This corresponds to disappearing of all spherical MOTSs. In contrast, if we gradually shrink the radius while keeping the mass and charge constant, the minimum shifts to $z_0 \rightarrow 0^+$ and simultaneously its value approaches $-\pi/2$. In this limit, θ_s has only one root since we are only interested in those roots that are non-negative (this is obvious since the ring with zero radius corresponds to the case of the Reissner–Nordström solution). However, figure 5.2a implies that in the case of vanishing radius there is a neighbourhood of $z_0 = 0$ in which θ_s is not defined. This “singular” behaviour is most probably not caused by non-existence of a solution for the given initial data, but rather by inaccuracy of our method. Indeed, when “shooting” the solution from the z -axis near the origin of the coordinate system, the numerical solution tends to be almost parallel to the equatorial plane at the point of intersection. Due to this effect supplemented by finite accuracy, it is possible that the numerical solution intersects the z -axis once again instead of crossing the equatorial plane, as the actual solution would do. However, there is also a possibility that, for a starting point that is too close to the singularity, the actual solution crosses the z -axis again after describing an arc. Nevertheless, based on our attempts at increasing the accuracy of the integration method, the former seems to be the case. Still, further investigation

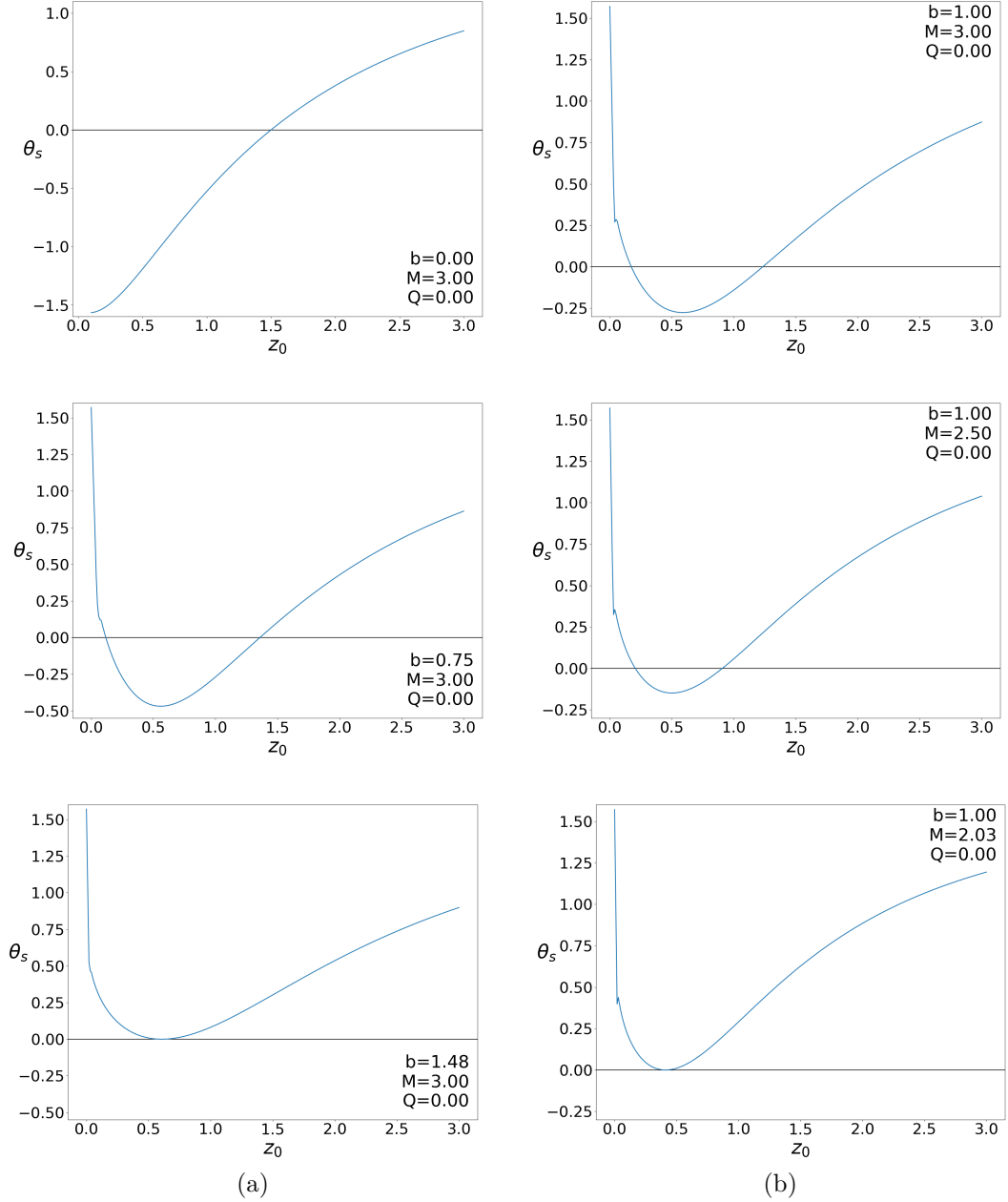


Figure 5.2: Dependence of θ_s on the initial guess of the position of a MOTS at the z -axis for families of hypersurfaces A and B , denoted by (a) and (b), respectively.

of this issue might prove fruitful. Interestingly, families B and C also exhibit the property of an extremal possible value of the free parameter. That is, for given values of b and Q , or b and M , there is a minimal value of M and a maximal value of Q , respectively, such that if these values are exceeded, there are no longer any spherical MOTSs around the ring. For our particular values of the family-defining parameters, these boundaries are $M_{\min} = 2.032369$ and $Q_{\max} = 2.123280$ (again, precise to six decimal places, not rounded). Similarly as in the preceding case, this phenomenon is illustrated in figure 5.2b. This behaviour is to some extent intuitive in the sense that if we stretch the radius without simultaneously increasing mass (or equivalently decrease the mass of the ring while keeping its radius constant), the mass density of the ring becomes too small to significantly affect space-time in its vicinity, and thus all spherical MOTS vanish. Also, regarding the maximal allowed value of the charge, similar situation

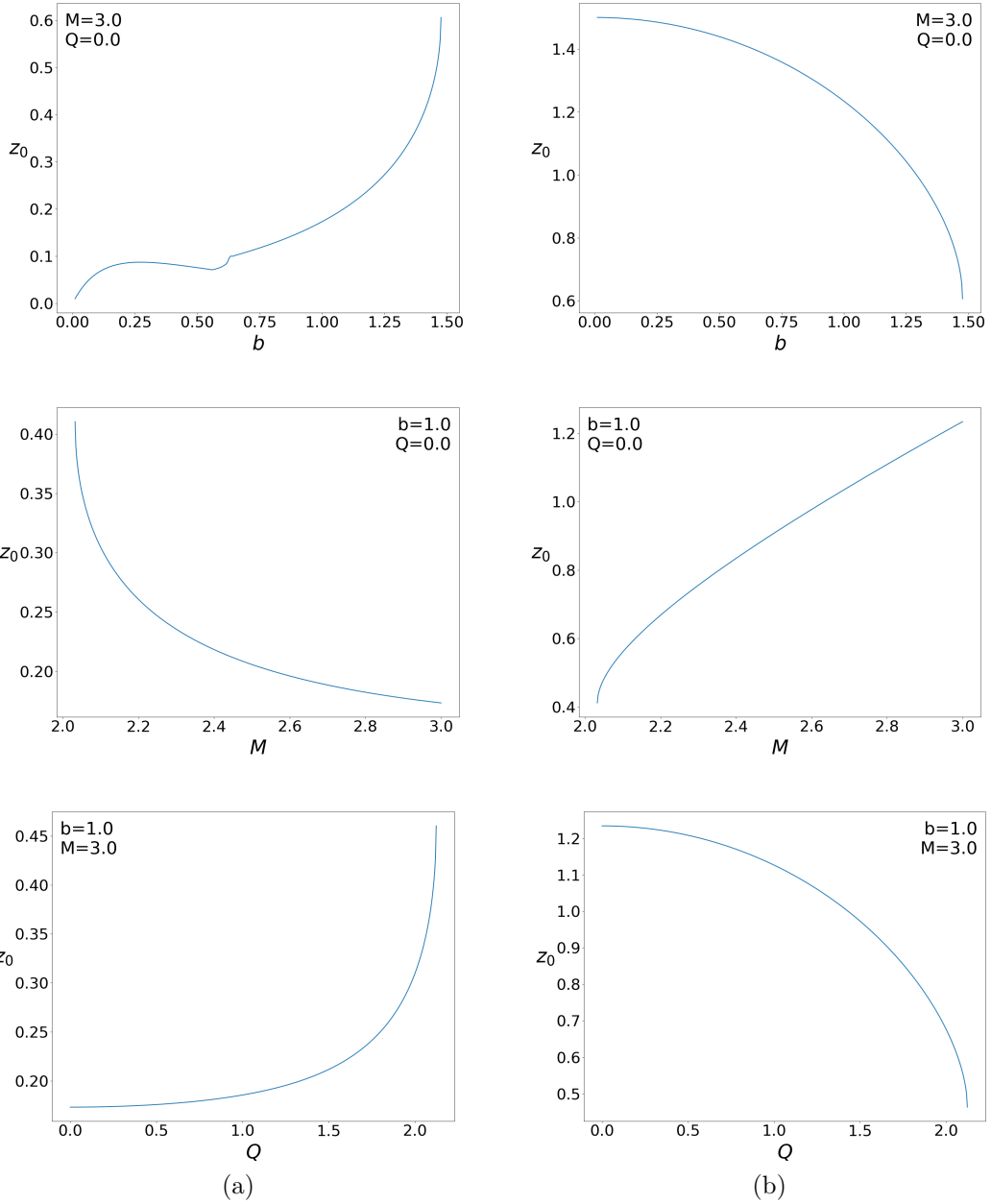


Figure 5.3: Dependence of the position of the inner (a) and outer (b) spherical MOTS at the z -axis on the values of the individual input parameters.

arises in the case of the Reissner–Nordström solution. Namely, it is a well-known property of static charged black holes that if the charge exceeds the mass, the event horizon vanishes. Consequently, the apparent horizon disappears as well. Thus, it only seems appropriate that if we keep the mass and radius constant as we increase the charge of the ring, a similar effect takes place. Moreover, if we set the constant radius to zero, the Reissner–Nordström case is perfectly reproduced, which makes the analogy even more obvious.

Finally, we were interested in how the “size” of the individual MOTSs depends on the family-defining parameters. By “size” we mean the location of the intersection of the individual MOTSs with the z -axis. Thus, it is clear that this notion is coordinate dependent and as such, it need not correspond to the actual “sizes” of the MOTSs. The obtained dependencies can be found in figures 5.3a and 5.3b,

respectively. It is worth noting that the inner and outer spherical MOTS have, in general, opposite slopes of growth within the same family of hypersurfaces, the only exception being a small interval of the rings' radii for which both MOTSs “shrink” when the rings expand.

5.3 Toroidal MOTSs

Besides spherical MOTSs, whose existence was strongly indicated by the correspondence of the rings with the Schwarzschild and Reissner–Nordström solutions in the limiting case of vanishing radius, one can also ask about MOTSs with toroidal topology due to the ring character of the Brill–Lindquist sources. Indeed, by employing the method of geodesics, we were able to determine that there exist such toroidal MOTSs and we found that their structure is often highly non-trivial.

In order to examine the conditions under which toroidal MOTSs form around the Brill–Lindquist rings, we used the same procedure as in the last section. Namely, we worked with three one-parameter families of hypersurfaces, denoted by A , B and C and defined in the same way as in Section 5.2. By adjusting the free parameter of each family, we managed to isolate intervals for which the rings admit toroidal MOTSs, provided the other parameters are kept constant. In general, these intervals further break up into subintervals determining the existence of the individual toroidal MOTSs. In addition, we plotted the dependences of θ_t on the initial value of ρ at the equatorial plane for particular members of the families so that we could illustrate basic characteristics of these surfaces. Lastly, we investigated the dependence of the MOTSs' ρ_0 on the values of the free parameter for each family. We summarize the obtained results in the following paragraphs.

Let us first take a look at figures 5.5–5.7 which imply that the behaviour of θ_t is far more complicated than that of θ_s . In order to understand the individual plots contained in these figures, it is necessary to specify a few more things concerning the roots of θ_t and their relation to the spherical MOTSs, as outlined in Section 5.1. Thus, consider the definition of θ_t which assigns the deviation from the right angle at which a solution “shot” orthogonally from the equatorial plane once again intersects the equatorial plane after describing an arc. The roots of this function define all the smooth surfaces with minimal area which intersect the equatorial plane orthogonally at each point. Nevertheless, spherical MOTSs also fulfill this requirement, so it may seem that localizing all the roots of θ_t should suffice to determine every single MOTS surrounding the ring (that is, not only those possessing toroidal topology). In principle, this should indeed be the case, but in practice this does not always work for numerical reasons, namely due to the singularity of the geodesic equation at the z -axis. Hence, if we try to “shoot” a solution from the equatorial plane with ρ_0 corresponding to a spherical MOTS, the numerical integration method fails to deliver a satisfactory result since the algorithm usually reports an error due to the singular behaviour near the z -axis. Therefore, it is clear that we need to eliminate these “singular” roots of θ_t from

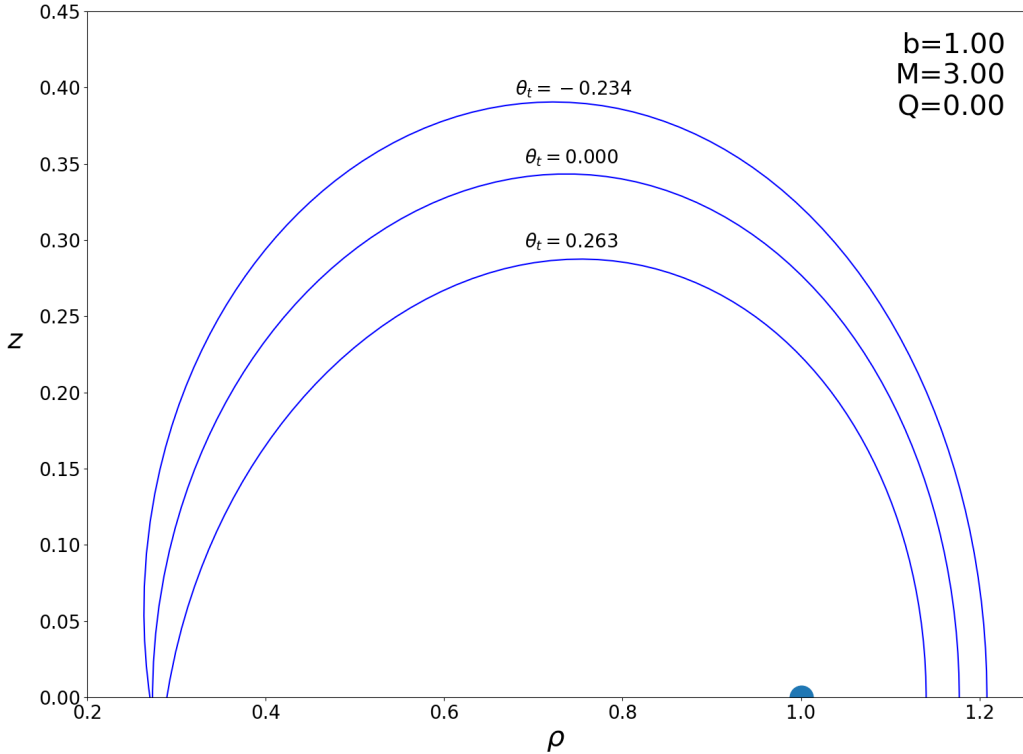


Figure 5.4: Illustration of the shooting algorithm searching for toroidal MOTSs in the case of the Brill–Lindquist rings with vanishing charge.

its domain before attempting to localize “regular” roots corresponding to the toroidal MOTSs.

As mentioned in the previous section, there are two spherical MOTSs in the most general case, and thus two “singular” roots. These roots then divide the domain of θ_t into three separate subintervals. In reality, the situation is even more complicated since, due to the inaccuracy of the numerical method, there are actually singular intervals around these ill-behaved roots (if we “shoot” a solution from a point that is too close to one of the “singular” roots, it can happen that both the “regular” and “singular” solution come so near to each other that the numerical method cannot distinguish between them anymore, and therefore such a solution also leads to an error). Fortunately, there is a simple solution to this problem. Namely, spherical MOTSs can be localized by the roots of θ_s independently on θ_t , and thus their intersections with the equatorial plane provide excellent estimates for the “singular” roots (the estimates are given by the vertical lines in figures 5.5–5.7). After obtaining approximate locations of these roots, it is not difficult to isolate the “singular” intervals surrounding them. Although the “singular” intervals are usually extremely narrow, it was not always possible to localize all the “regular” roots of θ_t without first removing these intervals from the function’s domain. In addition, the singular ring itself also lies in the equatorial plane and therefore it is required to exclude it, or rather a singular interval encapsulating it, from the domain of θ_t as well. The equatorial plane then breaks up into five concentric annuli obtained by removing those

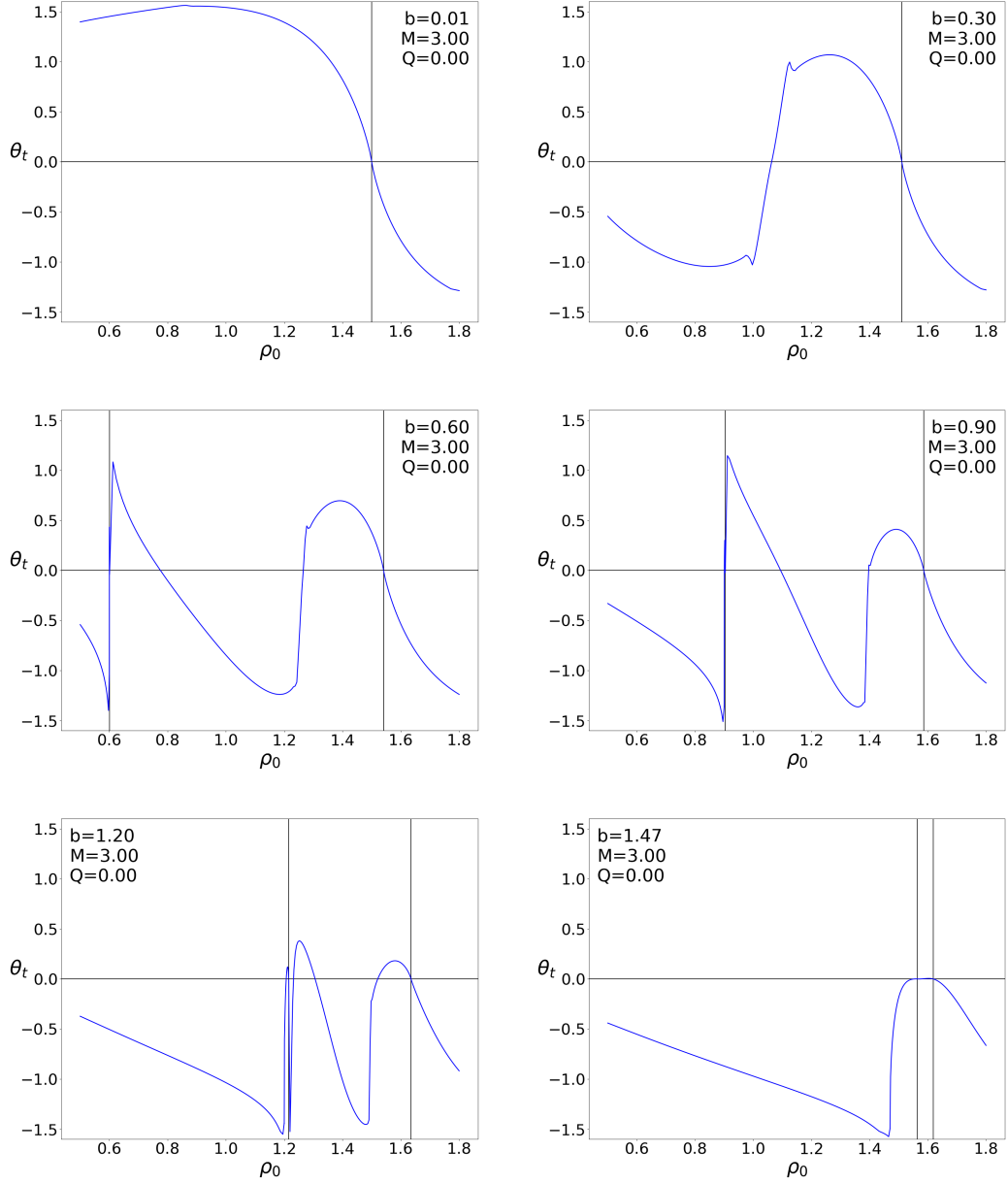


Figure 5.5: Dependences of θ_t on the initial value ρ_0 of solutions to the geodesic equation for the family of hypersurfaces with varying radius of the Brill–Lindquist ring.

intervals of ρ_0 that lead to an ill-behaved θ_t . In what follows, we present basic conclusions concerning the existence of toroidal MOTSs within the individual “regular” intervals of ρ_0 .

The most important seems to be a quite general observation that any Brill–Lindquist ring admits toroidal MOTSs only if there is a spherical apparent horizon surrounding all of them. That is, in all cases in which we managed to localize any toroidal MOTSs, they were always inside the outer spherical MOTS without intersecting it. Note that the opposite implication does not hold (there are such combinations of the input parameters for which there exists a spherical apparent horizon without any toroidal MOTSs inside it). This immediately implies that no toroidal apparent horizon was found for any of the three families of hypersurfaces. Concerning the families, this observation also significantly restricts the

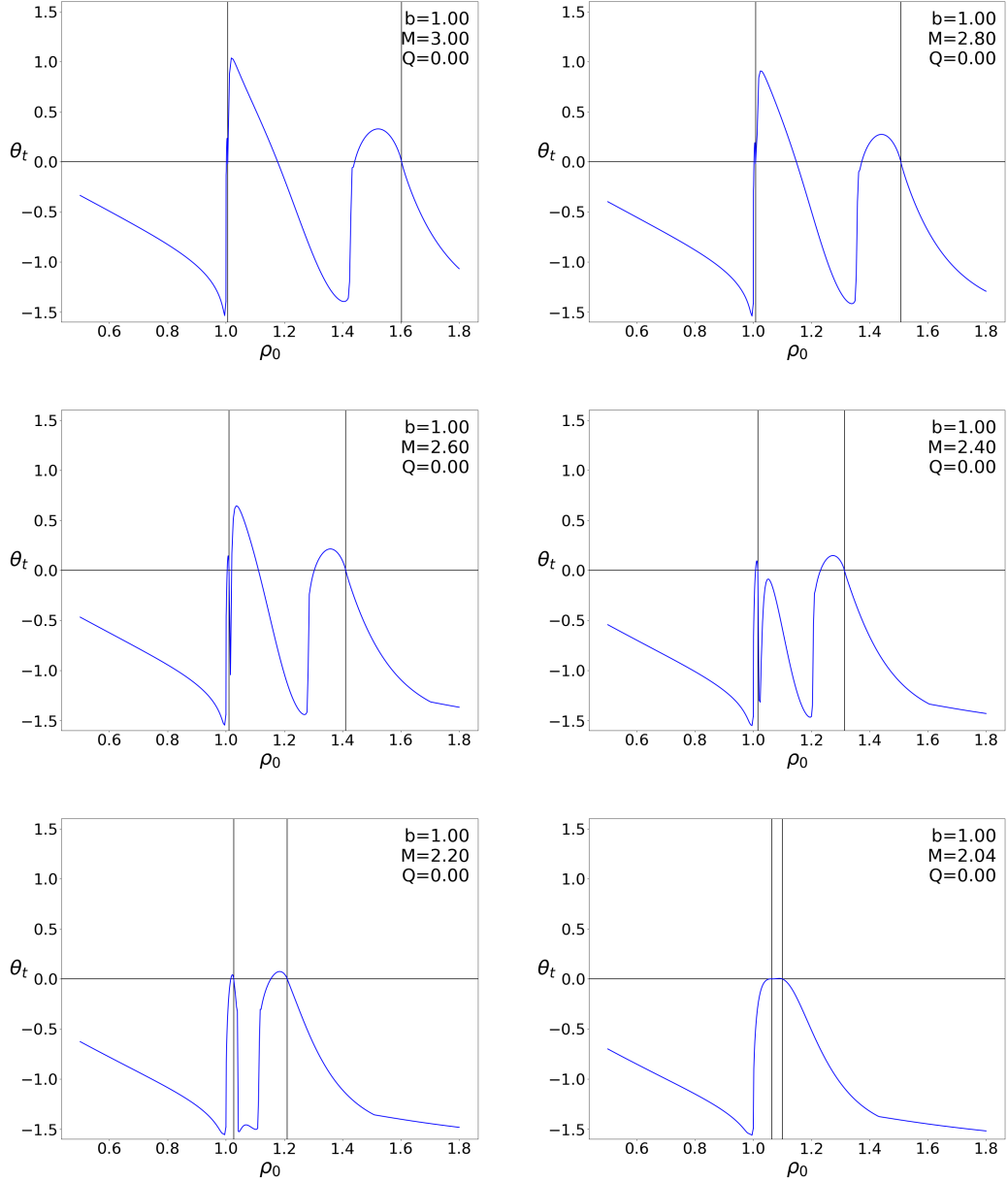


Figure 5.6: Dependences of θ_t on the initial value ρ_0 of solutions to the geodesic equation for the family of hypersurfaces with varying mass of the Brill–Lindquist ring.

allowed intervals of the free parameter to subintervals of those obtained for the spherical case. These intervals further break up into (in general intersecting) subintervals for the allowed values of the free parameter corresponding to the individual toroidal MOTS (as opposed to the spherical MOTSs which practically always exist in pairs, and thus their allowed intervals coincide). Consequently, for a given member of a family, it suffices to look for the roots of θ_t in the interval bounded from above by the position of the spherical apparent horizon at the equatorial plane, provided there is any. In addition, it is apparent that any toroidal MOTS must intersect the equatorial plane twice, and thus there are two roots of θ_t related to any such surface. Due to this fact, we do not have to localize all the “regular” roots but only those which lead to unique solutions of the geodesic equation. For instance, should each toroidal MOTS intersect the equatorial plane once on either side of the ring, it would be sufficient to localize only

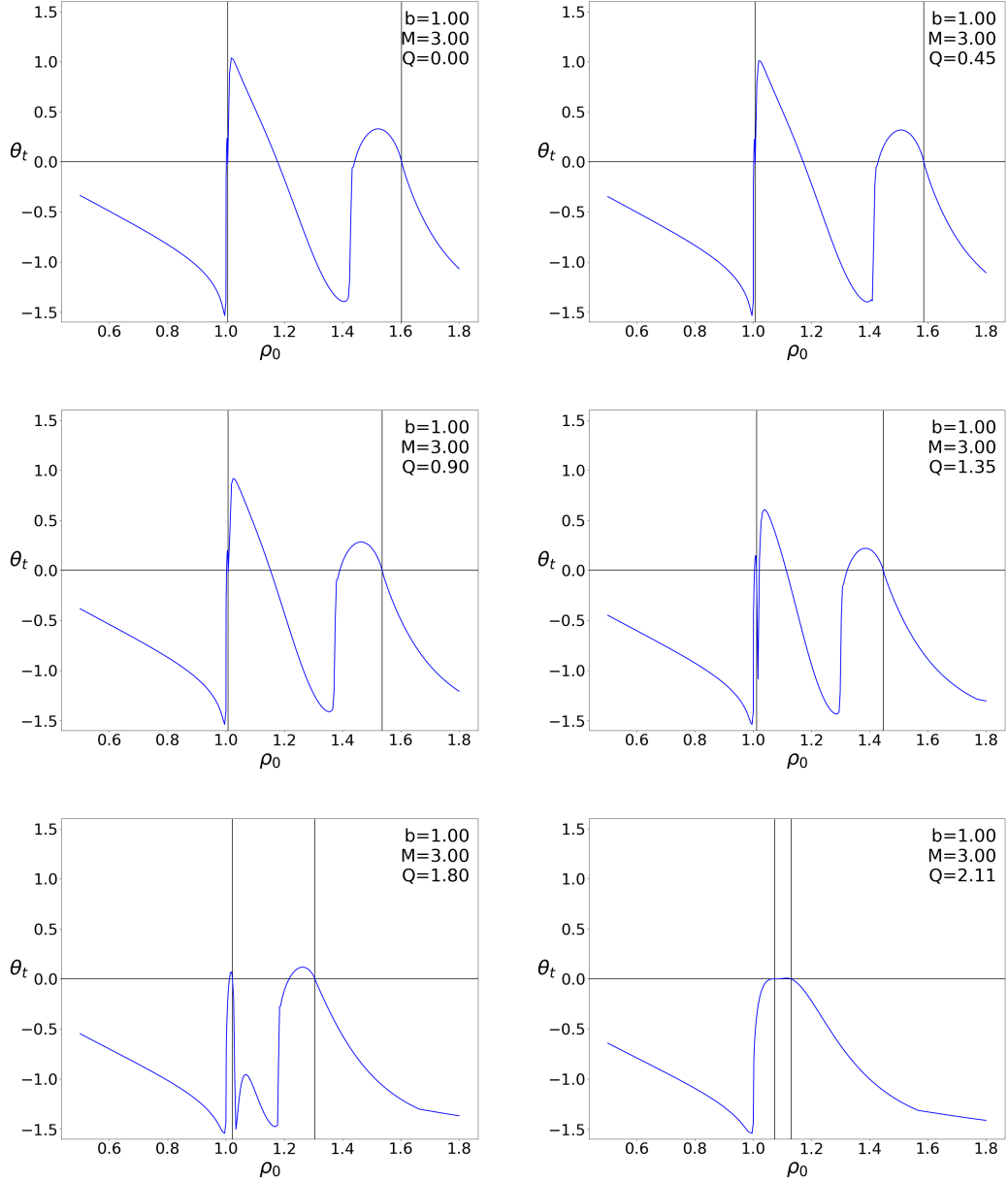


Figure 5.7: Dependences of θ_t on the initial value ρ_0 of solutions to the geodesic equation for the family of hypersurfaces with varying charge of the Brill–Lindquist ring.

the roots between the ring and the outer spherical MOTS. Indeed, this proved to be the correct conclusion, even though the assumption is not quite right. That is to say, there are toroidal MOTSs which intersect the equatorial plane twice on the same side of the ring. However, based on our results, the intersection points of such MOTSs, quite generally, lie between the ring and the spherical apparent horizon, and thus it actually suffices to find the “regular” roots corresponding to unique solutions in this interval (therefore, figures 5.5–5.7 focus on the shapes of θ_t especially in such intervals). It can be shown that in the most general case there are four roots of interest. Nevertheless, only three of them lead to a unique solution to the geodesic equation, thus defining a separate toroidal MOTS. Figures 5.5–5.7 illustrate the “evolution” of the individual roots with respect to the free parameter of the three families.

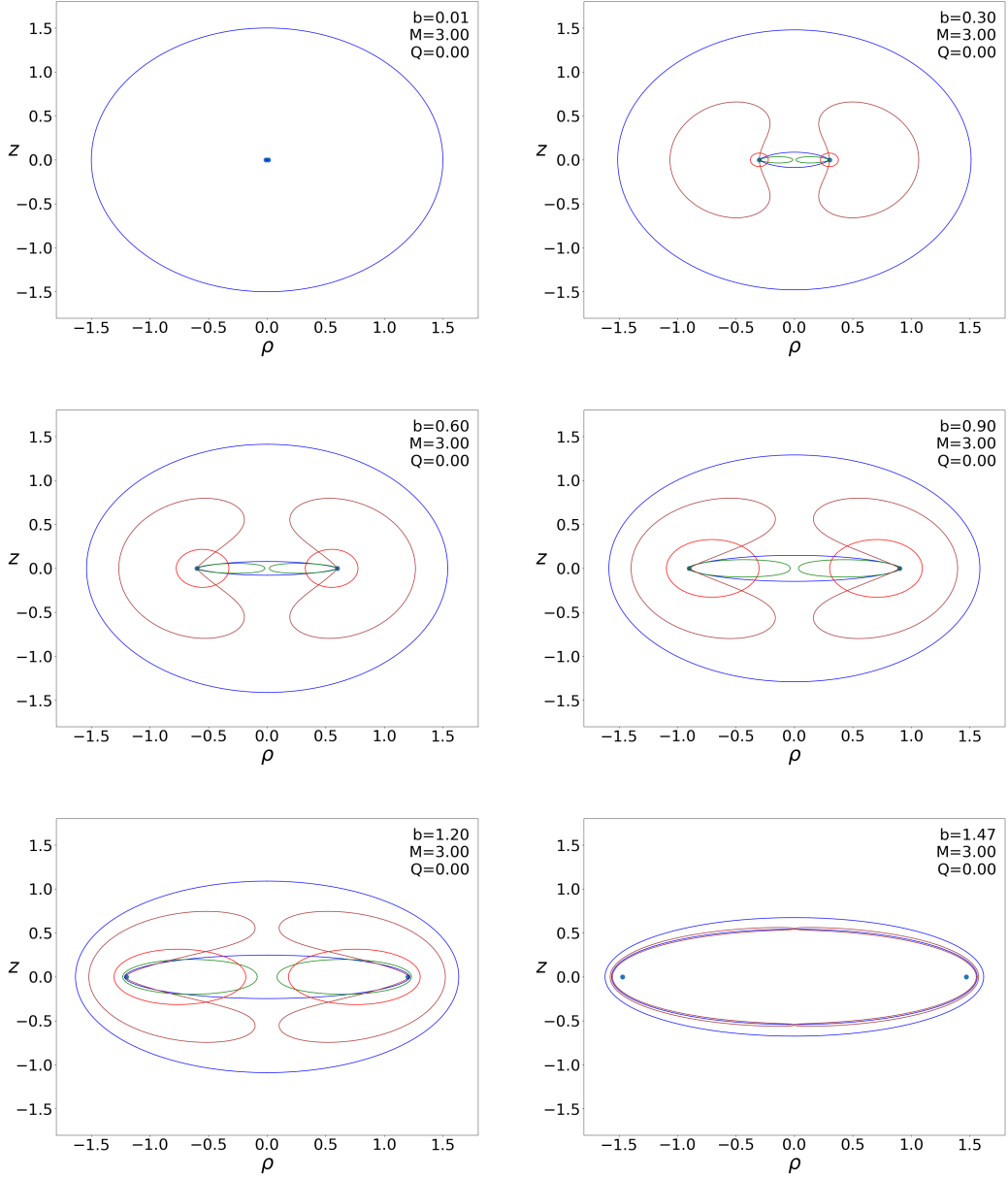


Figure 5.8: Coordinate shapes of the marginally outer-trapped surfaces surrounding the Brill–Lindquist rings with varying radius.

Let us now point out a few conclusions which follow from these dependences. First, in the case of family *A* (see figure 5.5), it is apparent that for the radius tending to zero, all toroidal MOTSs vanish. This is to be expected since this limiting case corresponds to the Reissner–Nordström solution which is known to possess no toroidal MOTSs. As we gradually expand the radius of the ring, a first toroidal MOTS appears at approximately $b = 0.05$. If we continue to expand the ring, eventually two more MOTSs emerge at the “same time” in analogy with the paired existence of the two spherical MOTSs. This property of the two related toroidal MOTSs turns out to be quite general as they always appear and disappear together (within the tolerance of the numerical method). Indeed, when the ring’s radius exceeds the value $b = 1.24$, the two emergent MOTSs vanish as predicted. Finally, for the radius of approximately $b = 1.47$, the last toroidal MOTS also disappears. However, as opposed to the preceding case, this is probably caused by the inaccuracy of our method rather than the actual vanishing of the MOTS. The

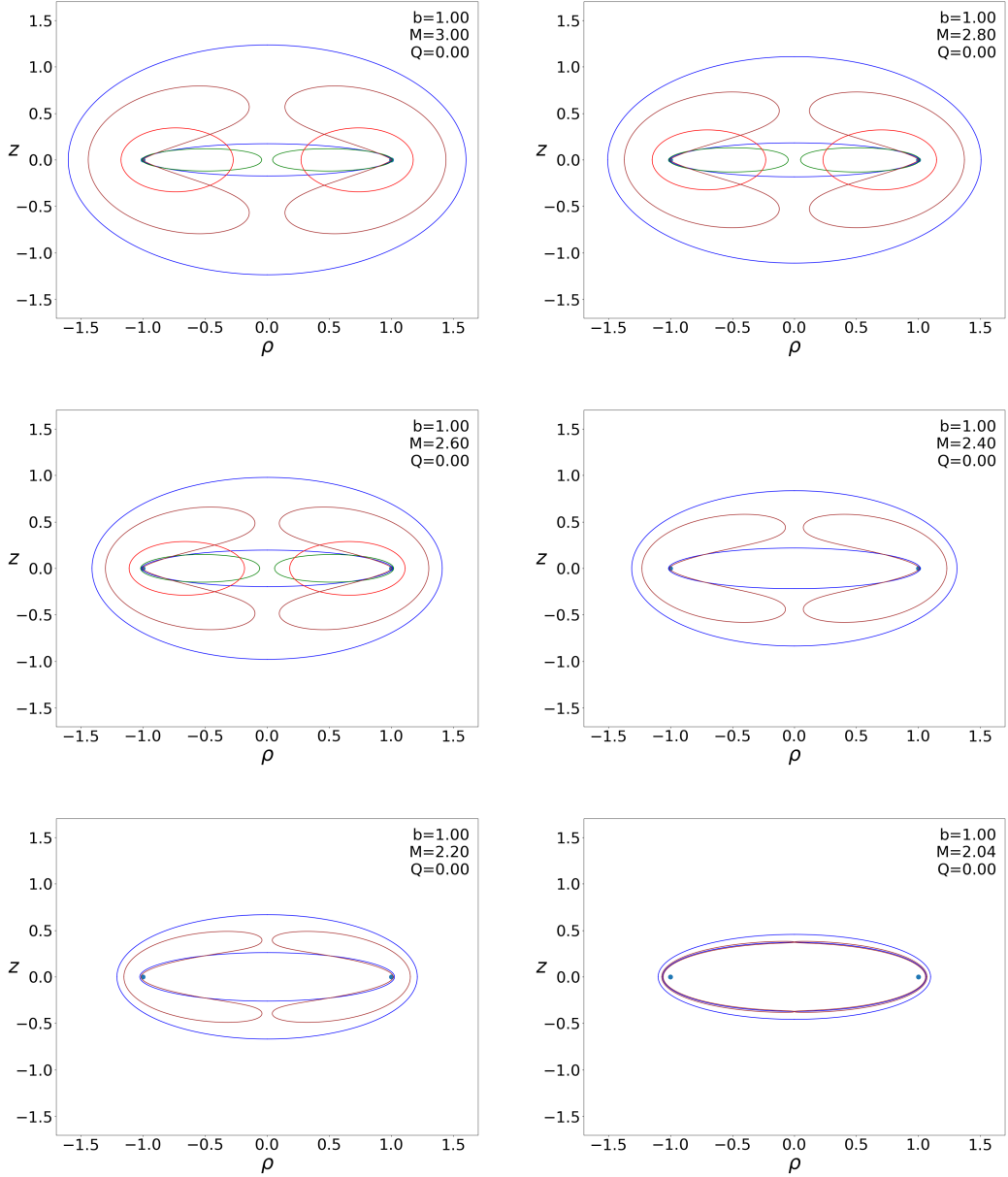


Figure 5.9: Coordinate shapes of the marginally outer-trapped surfaces surrounding the Brill–Lindquist rings with varying mass.

reason for this is that as the radius expands, the root corresponding to the last toroidal MOTS shifts toward the smaller “singular” root, as can be seen in figure 5.5. Thus, it is possible that the “regular” root enters the artificial “singular” interval before the toroidal MOTS actually disappears (this possibility is also supported by the shapes of the individual MOTSs just before their vanishing as briefly discussed at the end of this section). In addition, figures 5.6 and 5.7 imply that the “evolution” of θ_t with respect to decreasing mass (family *B*) and increasing charge (family *C*) is qualitatively the same. Namely, as we shift the free parameter from its initial to its final value, the corresponding MOTSs go through similar phases as in the case of the expanding radius (except for the initial phases of no and one toroidal MOTS). The last toroidal MOTSs disappear as the mass and charge exceed the values $M_{\min} = 2.04$ and $Q_{\max} = 2.11$, respectively. The remark on the inaccuracy of the integration method as a possible cause of their premature vanishing applies here as well, and thus further investigation of

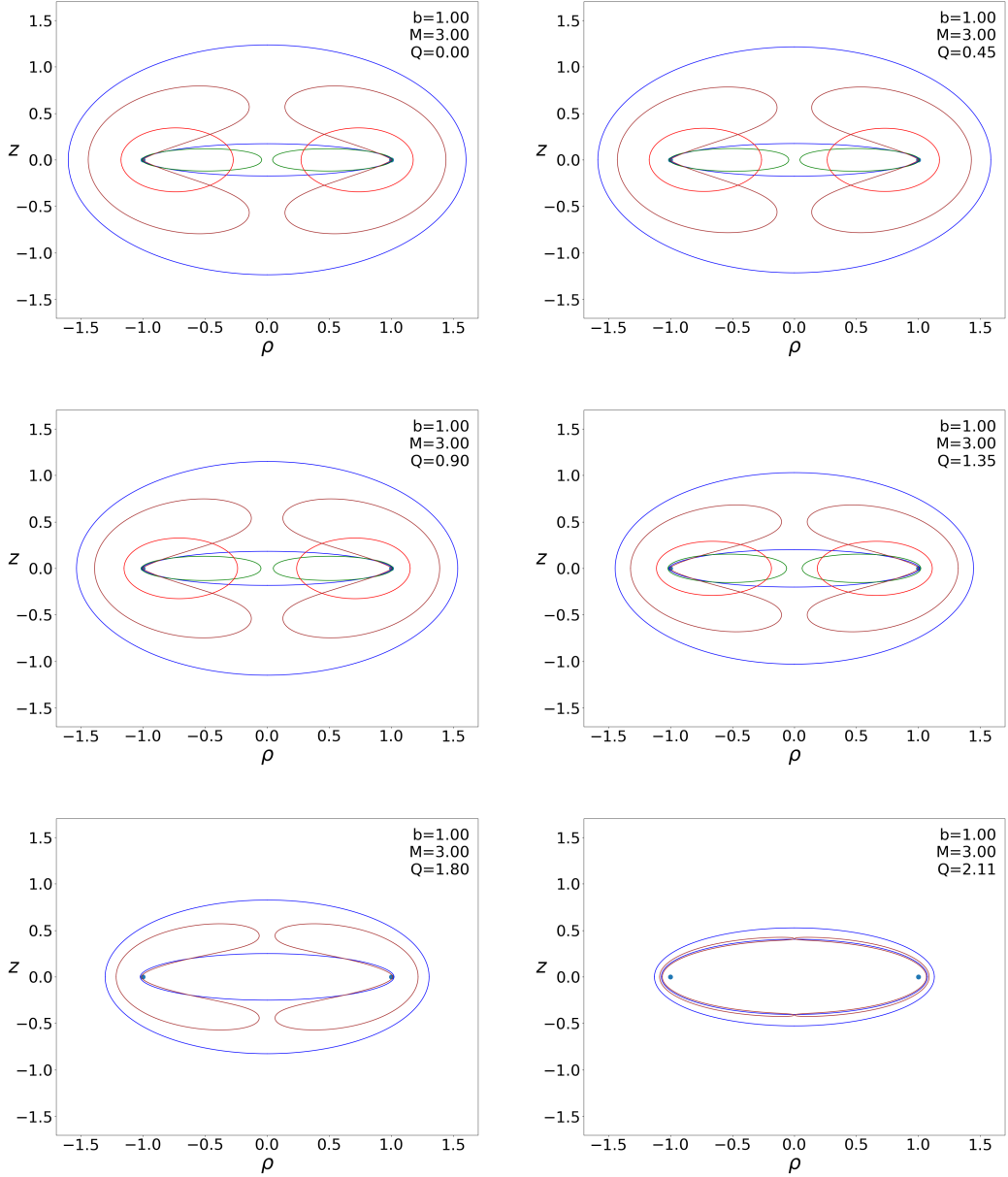


Figure 5.10: Coordinate shapes of the marginally outer-trapped surfaces surrounding the Brill–Lindquist rings with varying charge.

this phenomenon using more accurate numerical integration methods might be appropriate (note that we could also argue for the delayed appearance of toroidal MOTSs using the same reasoning).

Having described the development of the individual toroidal MOTSs along the free parameters of the families, let us illustrate these results by showing the coordinate shapes of the surfaces. Since the existence of toroidal MOTSs is closely related to spherical apparent horizons, it is natural to show the whole system of both spherical and toroidal MOTSs at once. Figures 5.8–5.10 illustrate the dependence of such a system of surfaces, specifically the dependence of their cross-sections in any meridian plane, on the radius, mass and charge of the Brill–Lindquist rings. Note that for all figures, the extremal value of the respective parameter corresponds to vanishing of the last toroidal MOTS. The figures further imply that a general situation is quite complicated, with multiple MOTSs intersecting each

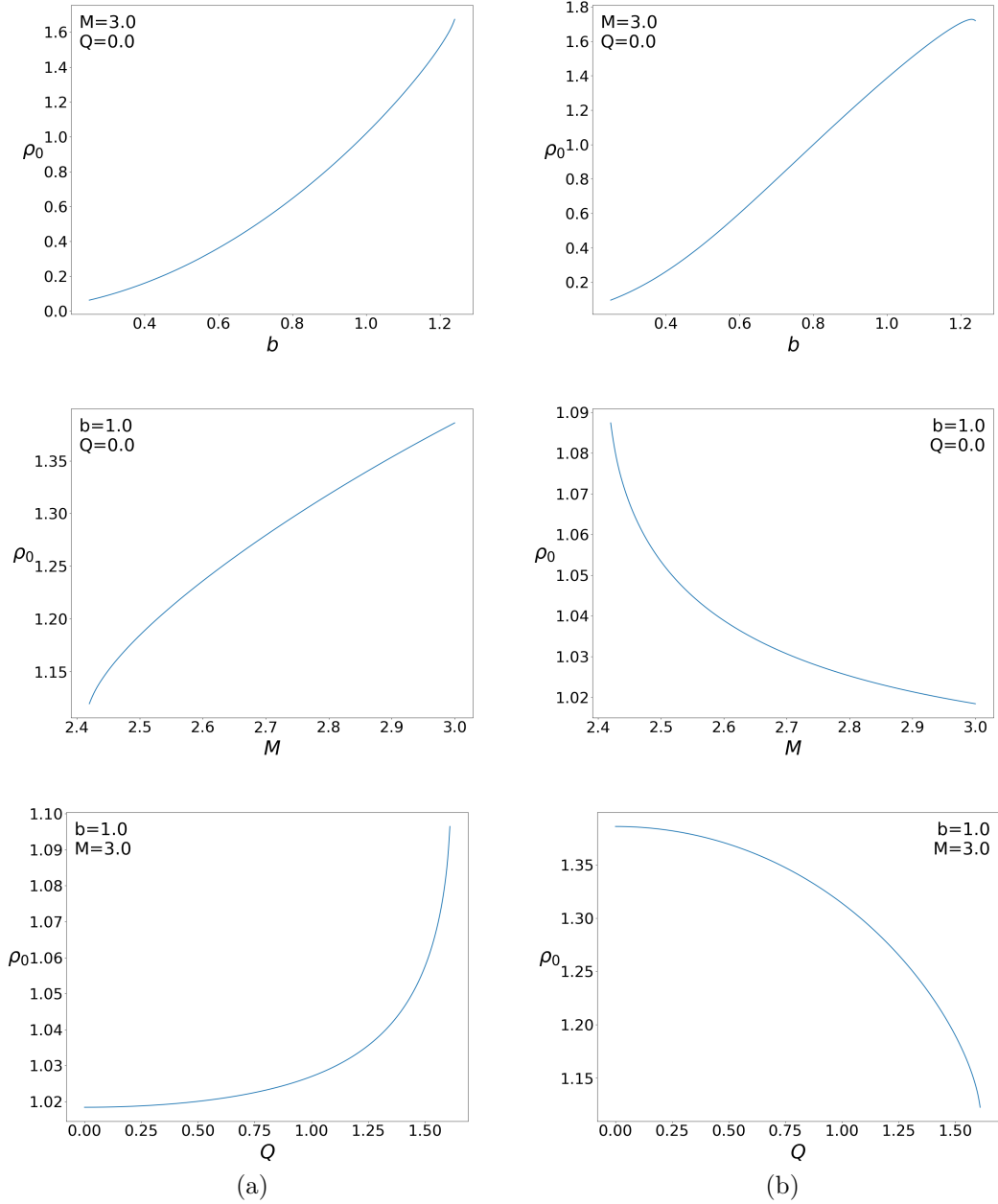


Figure 5.11: Dependence of the initial value of ρ at the equatorial plane for the inner (a) and central (b) toroidal MOTS on the parameters of the three families.

other several times. Hence, it is necessary to be able to differentiate between the individual surfaces before proceeding any further. Based on figures 5.8–5.10, we will refer to the green, red and brown toroidal MOTS as the inner, the central and the outer toroidal MOTS (the distinction between the outer and inner spherical MOTS is apparent). Using this notation, we are now able to describe the process of appearing and disappearing of toroidal MOTSs in more detail. Let us first restrict our attention to the case of family *A* which is depicted in figure 5.8. Clearly, in the limiting case of vanishing radius, the whole system of MOTSs reduces to the single apparent horizon of the Reissner–Nordström solution, as already mentioned. Although not shown in figure 5.8, it can be proven that as the radius of the ring gradually expands, only the outer toroidal MOTS starts to grow around the singularity at first. After the ring radius reaches a certain value, the inner and central toroidal MOTSs appear as well. Most notably, figure 5.8

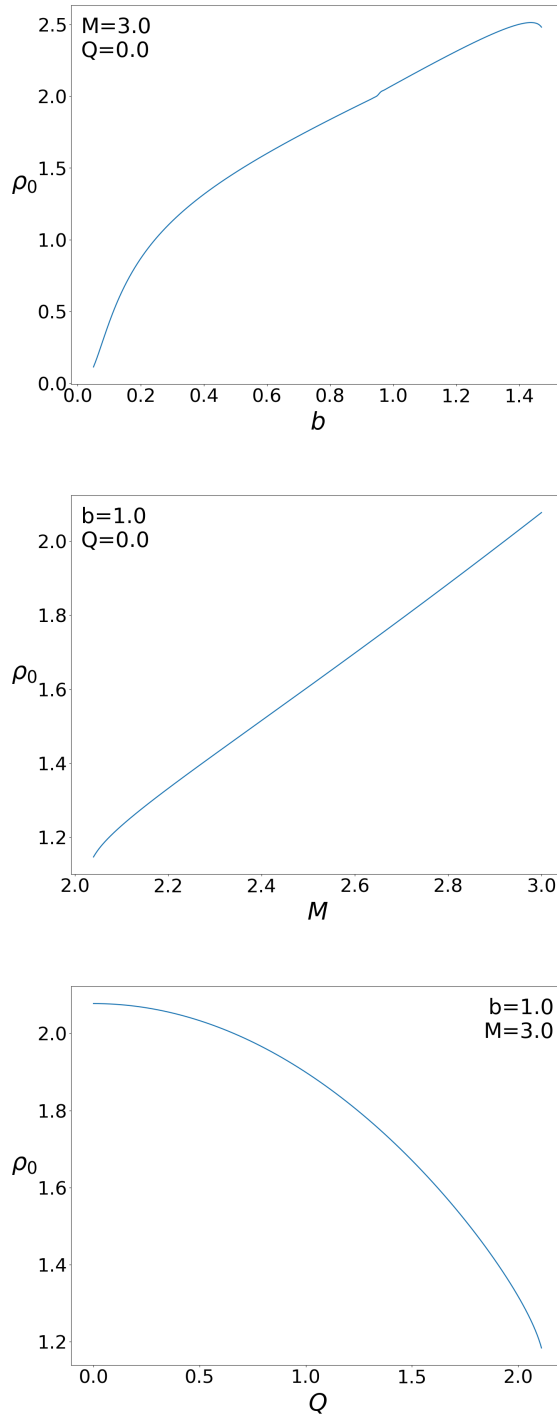


Figure 5.12: Dependence of the initial value of ρ at the equatorial plane for the outer toroidal MOTS on the parameters of the three families.

further implies that as the radius approaches its maximal allowed value, the outer toroidal MOTS is continuously deformed into a third “spherical” MOTS, partly enclosed by the inner and outer spherical MOTSs. Note that figures 5.9 and 5.10 show the same behaviour for families B and C as the mass and charge of the ring tend to their extremal values. This behaviour of the outer toroidal MOTS further suggests that its vanishing before the merger of the two spherical MOTSs could be just of numerical character due to inaccuracy of the numerical method. If that were the case, we would expect (regarding the shapes of the MOTSs near the extremal values of free parameters) that the outer toroidal MOTS actually merges with the two spherical MOTSs into a single spherical apparent horizon

just before the latter finally vanishes. Naturally, this is just an assumption that should be verified by more accurate numerical tools.

Finally, using the unique identification of the toroidal MOTSs, figures 5.11 and 5.12 show the dependences of their ρ_0 (in the interval between the ring singularity and the spherical apparent horizon) on the radius, mass and charge of the Brill–Lindquist ring for the three families of hypersurfaces. Note that in the case of the outer toroidal MOTS which intersects the interval twice, we considered the larger of the two roots of θ_t .

5.4 Final remarks

Although we constructed the Brill–Lindquist rings with the help of the initial data corresponding to a system of multiple charged black holes initially at rest, it is not reasonable to expect that this interpretation is also applicable to the case of the rings. The reason for this is that in their derivation we considered the limiting case of an infinite number of infinitesimally separated “punctures” rather than a spatially sufficiently separated finite system of “particles” for which the black hole interpretation holds. Thus, in order to gain an insight into possible physical representations of the Brill–Lindquist rings, it is advisable to examine some of the invariant characteristics of these hypersurfaces.

To illustrate this process, consider the special case of an extremal ring, whose mass equals the absolute value of its charge, investigated by Semerák (2016). The conformal factor of the corresponding hypersurface is given by

$$\Omega = \sqrt{1 + \frac{M}{\pi} \left[\frac{K\left(-\frac{4\rho b}{z^2 + (\rho - b)^2}\right)}{\sqrt{z^2 + (\rho - b)^2}} + \frac{K\left(\frac{4\rho b}{z^2 + (\rho + b)^2}\right)}{\sqrt{z^2 + (\rho + b)^2}} \right]}, \quad (5.3)$$

as can be easily seen from equations (3.16a) and (3.16b). In the mentioned paper, the metric describing such an extremal ring is derived using the Majumdar-Papapetrou solution representing a system of charged black holes in equilibrium under their gravitational and electrical forces rather than our method based on the Brill–Lindquist initial data. Nevertheless, both approaches yield the same results, even though our choice leads to a more general situation of arbitrarily charged rings. Furthermore, if we adopt the paper’s definition of the complete elliptic integral of the first kind (compare with equation (3.17)) for the rest of this chapter, that is

$$K(k) = \int_0^{\pi/2} \frac{1}{\sqrt{1 - k^2 \sin^2 \alpha}} d\alpha, \quad (5.4)$$

the conformal factor can be rewritten as

$$\Omega = \sqrt{1 + \frac{2MK\left(2\sqrt{\frac{b\rho}{z^2 + (\rho + b)^2}}\right)}{\pi\sqrt{z^2 + (\rho + b)^2}}}. \quad (5.5)$$

In the following paragraphs, we present a brief summary of the basic results concerning the extremal Brill–Lindquist rings (which are referred to as the Majumdar-Papapetrou rings, or the M-P rings for short) obtained in the original paper.

First, by employing toroidal coordinates (ζ, ψ, ϕ) related to cylindric coordinates by

$$\rho = \frac{b \sinh \zeta}{\cosh \zeta - \cos \psi}, \quad z = \frac{b \sin \psi}{\cosh \zeta - \cos \psi}, \quad (5.6)$$

where $\zeta \in [0, +\infty)$ and $\psi \in [0, 2\pi)$, it can be shown that the circumference l_1 of any $\zeta = \text{const.}$ tube amounts to

$$l_1 = 2 \int_0^\pi \sqrt{h_{\psi\psi}} \, d\psi = 2b \int_0^\pi \frac{\Omega^2}{\cosh \zeta - \cos \psi} \, d\psi \quad (5.7)$$

$$= \frac{2\pi b}{\sinh \zeta} + \frac{4\sqrt{2}MK(\sqrt{1 - e^{-2\zeta}})}{\pi e^{\zeta/2} \sqrt{\cosh \zeta + 1}} K\left(\frac{\sqrt{2}}{\sqrt{\cosh \zeta + 1}}\right). \quad (5.8)$$

In the limit $\zeta \rightarrow +\infty$ which corresponds to the singular ring, the cross circumference of the M-P ring tends to zero. Furthermore, the circumferential radius of the ring, denoted by r_c and given by

$$r_c = \lim_{\zeta \rightarrow +\infty} \sqrt{g_{\phi\phi}} = b + \frac{M}{\pi} \lim_{\zeta \rightarrow +\infty} K(\sqrt{1 - e^{-2\zeta}}), \quad (5.9)$$

diverges, and thus the “large” circumference $l_2 = 2\pi r_c$ diverges as well (except for the case of vanishing radius). The proper radius r_p of the ring equals

$$r_p = b + \frac{4\mathcal{G}}{\pi} M, \quad (5.10)$$

where

$$\mathcal{G} = \frac{1}{2} \int_0^1 K(v) \, dv \approx 0.9159656$$

is Catalan’s constant. Equation (5.10) then implies that the proper radius is finite for all non-zero values of b as opposed to the circumferential radius. Finally, the proper area A of any such a ring is also finite as it amounts to

$$A = \pi b^2 + 8Mb + \frac{14\zeta(3)}{\pi} M^2, \quad (5.11)$$

where

$$\zeta(3) = \frac{4}{7} \int_0^1 vK(v) \, dv = \sum_{n=1}^{+\infty} \frac{1}{n^3} \approx 1.2020569$$

corresponds to the Riemann zeta function evaluated at the value of 3 and is known as Apéry’s constant.

The original paper further derives expressions for such quantities as the Kretschmann invariant, the Gauss curvature of various planes or “gravitational acceleration”. In particular, it can be shown that the Kretschmann invariant diverges in the vicinity of the M-P ring, and thus, at least in the case of the extremal charge, the ring singularity is in fact genuine. Investigation of similar properties in the case of a generic Brill–Lindquist ring might be a fruitful object of further study.

Lastly, note that the question of spherical MOTSs surrounding the Brill–Lindquist rings for the uncharged case was already examined by Jaramillo and Lousto (2011). In this paper, they employ the method of geodesic as well. However, their implementation of the shooting algorithm uses some sort of a “visual” method to localize the roots of their equivalent of θ_t . Consequently, the obtained results concerning the location of the spherical apparent horizon do not seem to correspond to our findings. More precisely, for each value of the mass of the ring, they managed to localize only one spherical MOTS (to which they refer as the apparent horizon) whose position at the z -axis does not match our values for either of the two spherical MOTSs. Clearly, this inconsistency of the results is surely worth further investigation.

Conclusion

In this thesis, we studied the spaces of massive charged thin rings obtained as a certain limit of multiple-black-hole configurations described by the Brill–Lindquist initial-data metrics. Our interest in ring solutions mainly arises from a “hope” that ring sources could give rise to toroidal horizons. Another motivation comes from the paper by Jaramillo & Lousto (2011) who analysed the occurrence of (spheroidal) horizons around an uncharged case of the studied rings, as their conclusions did not seem very convincing.

More specifically, we started from the Brill–Lindquist initial data and created a system of time- and axially symmetric conformally flat hypersurfaces with additional reflection symmetry, by arranging the “punctures” of the metric (originally representing black holes) in a circle and considering the limiting case of an infinite number of them. In such a way, one obtains spaces which are singular at circular rings characterized by their radius, mass and charge. We did not investigate the actual nature of these rings, but there is some evidence that they correspond to genuine physical singularities. We then checked for the existence and character of apparent horizons (more accurately, marginally outer-trapped surfaces, or MOTS) around the constructed Brill–Lindquist rings. Namely, it is a well-known property of apparent horizons that, under right circumstances, they approximate the spatial “snapshot” of an event horizon at a certain instance of time. Thus, if toroidal apparent horizons were to be found in these hypersurfaces, the corresponding space-times obtained by evolving them would serve as candidates for containing toroidal event horizons.

Using our implementation of the method of geodesics, we verified that toroidal MOTSs indeed do form around the Brill–Lindquist rings, provided that the rings’ parameters lie in certain intervals. However, we did not manage to find a case with a toroidal apparent horizon, because all the toroidal MOTSs were always contained within a spherical MOTS, and thus only spherical apparent horizons (the outermost MOTS) were found. Furthermore, the system of spherical and toroidal MOTSs proved to be rather complicated, with multiple extremal surfaces intersecting each other. In order to investigate their dependences on the input parameters, we introduced three families of hypersurfaces parametrized by the ring’s radius, mass and charge, respectively. For each family we localized the interval of the free parameter for which the individual MOTSs exist. Interestingly, we found that there is a maximal value of the ring’s radius such that if it is exceeded, no MOTSs of either topology were found, provided that the other parameters were kept constant. Similar behaviour was also observed for the mass and charge of the ring. Namely, there is a certain minimal value of mass and a maximal value of charge such that no minimal surfaces of either topology were localized if the free parameters exceeded these values while the other were kept constant. Note that both the radius and the charge of the ring are in general also bounded from below – the former by definition and the latter due to the symmetry of the line element with respect to changing the sign of the charge. In addition, we examined the shapes of the minimal surfaces and by focusing on

their deformation near the extremal values of the free parameters, we illustrated probable shortcomings of the employed numerical method. Finally, we added a brief discussion on the character and properties of the extremal Brill–Lindquist ring and pointed out the inconsistency of the obtained results with those published (for an uncharged ring) by Jaramillo & Lousto.

At several places, we indicated what could be the directions of further study. Let us briefly repeat here that, first, the Brill–Lindquist rings were obtained as a certain limit of spaces originally interpreted as a system of black holes, but finally representing a singular ring. This latter interpretation should be taken with caution and further investigation of such rings is certainly required. Furthermore, there are several numerical issues. In particular, seeing that our functions θ_s and θ_t , crucial for the localization of MOTSs, in fact correspond to an imprecise representation of the actual functions (which are enclosed within the interval of the required accuracy about the approximate solutions), there is no guarantee that the localized roots are indeed precise to six decimal places (or to any other accuracy that we could require) as the actual error depends on the slopes of the *precise* functions. Regarding the shapes of θ_s and θ_t , though, the only possible case of accuracy loss seem to be the shallow minima corresponding to the merger of the two spherical MOTSs. Although we checked the basic numerical calculations by the Mathematica program, verification of the results using an independent method would be appropriate, the more so that our results differ considerably from those obtained by Jaramillo & Lousto (2011). And finally, it should be kept in mind that the Brill–Lindquist rings define certain initial data and, as such, they call for being numerically evolved, since it might be interesting to track the evolution of the individual MOTSs, or eventually investigate the character of the event horizon that is expected to form around the singular rings (a more general method would certainly be required to perform such a task, because the employed method only applies to time-symmetric hypersurfaces).

Bibliography

- T. W. Baumgarte and S. L. Shapiro. *Numerical relativity*. Cambridge University Press, New York, 2010. ISBN 978-0-511-72937-9.
- D. R. Brill and R. W. Lindquist. Interaction energy in geometrostatics. *Phys. Rev.*, 131:471–476, Jul 1963. doi: 10.1103/PhysRev.131.471. URL <https://link.aps.org/doi/10.1103/PhysRev.131.471>.
- B. Carter. Axisymmetric Black Hole Has Only Two Degrees of Freedom. *Phys. Rev. Lett.*, 26:331–333, 1971. doi: 10.1103/PhysRevLett.26.331.
- S. W. Hawking. Black holes in general relativity. *Comm. Math. Phys.*, 25(2):152–166, 1972. URL <https://projecteuclid.org:443/euclid.cmp/1103857884>.
- S.W. Hawking and G.F.R. Ellis. *The large scale structure of space-time*. Cambridge University Press, Cambridge, 1994. ISBN 0-521-09906-4.
- W. Israel. Event horizons in static vacuum space-times. *Phys. Rev.*, 164:1776–1779, Dec 1967. doi: 10.1103/PhysRev.164.1776. URL <https://link.aps.org/doi/10.1103/PhysRev.164.1776>.
- W. Israel. Event horizons in static electrovac space-times. *Comm. Math. Phys.*, 8(3):245–260, 1968. URL <https://projecteuclid.org:443/euclid.cmp/1103840605>.
- G. Jaramillo and C. O. Lousto. Study of multi black hole and ring singularity apparent horizons. *Phys. Rev. D*, 84:104011, 2011. doi: 10.1103/PhysRevD.84.104011.
- N. Lages. *Apparent Horizons and Marginally Trapped Surfaces in Numerical General Relativity*. PhD thesis, Friedrich Schiller University Jena, 2010.
- R. Leveque. *Finite Difference Methods for Ordinary and Partial Differential Equations: Steady-State and Time-Dependent Problems*. Society for Industrial and Applied Mathematics, Philadelphia, 2007. ISBN 978-0-898716-29-0.
- P. O. Mazur. Proof of uniqueness of the Kerr-Newman black hole solution. *J. Phys. A: Math. Gen.*, 15(10):3173–3180, 1982. URL <http://stacks.iop.org/0305-4470/15/i=10/a=021>.
- E. Poisson. *A RELATIVIST'S TOOLKIT*. Cambridge University Press, Cambridge, 2004. ISBN 0-521-83091-5.
- W. H. Press, S. A. Teukolsky, W. T. Vetterling, and B. P. Flannery. *Numerical Recipes 3rd Edition: The Art of Scientific Computing*. Cambridge University Press, Cambridge, 2007. ISBN 978-0-511-33555-6.
- D. C. Robinson. Uniqueness of the Kerr black hole. *Phys. Rev. Lett.*, 34:905–906, Apr 1975. doi: 10.1103/PhysRevLett.34.905. URL <https://link.aps.org/doi/10.1103/PhysRevLett.34.905>.
- O. Semerák. Static axisymmetric rings in general relativity: How diverse they are. *Phys. Rev. D*, 94(10):104021, 2016. doi: 10.1103/PhysRevD.94.104021.
- J. Thornburg. Event and apparent horizon finders for 3+1 numerical relativity. *arXiv:gr-qc/0512169v2*, 2006.
- R. M. Wald. *General Relativity*. The University of Chicago Press, Chicago, 1984. ISBN 0-226-87033-2.